UCRL-2153

UNCLASSIFIED

UNIVERSITY OF CALIFORNIA — BERKELEY

TWO-WEEK LOAN COPY

This is a Library Circulating Copy which may be borrowed for two weeks. For a personal retention copy, call Tech. Info. Division, Ext. 5545

RADIATION LABORATORY

UCRL-2153 C.2

DISCLAIMER

This document was prepared as an account of work sponsored by the United States Government. While this document is believed to contain correct information, neither the United States Government nor any agency thereof, nor the Regents of the University of California, nor any of their employees, makes any warranty, express or implied, or assumes any legal responsibility for the accuracy, completeness, or usefulness of any information, apparatus, product, or process disclosed, or represents that its use would not infringe privately owned rights. Reference herein to any specific commercial product, process, or service by its trade name, trademark, manufacturer, or otherwise, does not necessarily constitute or imply its endorsement, recommendation, or favoring by the United States Government or any agency thereof, or the Regents of the University of California. The views and opinions of authors expressed herein do not necessarily state or reflect those of the United States Government or any agency thereof or the Regents of the University of California.

UCRL-2153
Unclassified-Physics Distribution

UNIVERSITY OF CALIFORNIA
Radiation Laboratory

Contract No. W-7405-eng-48

A HIGH-PRESSURE CLOUD-CHAMBER INVESTIGATION OF PROTONS SCATTERED BY 300 MEV NEUTRONS

John De Pangher, Jr.

(Thesis)

March 17, 1953

Berkeley, California

TABLE OF CONTENTS

		Page No.
ABSTRACT		4
1.	INTRODUCTION	5
2.	THE TEN-ATMOSPHERE WILSON CLOUD CHAMBER	8
	A. General Features of Construction	8
	B. The Gas Control System	14
	C. Photography	17
	D. Magnet	19
	E. Temperature Control	19
	F. Synchronization of Cloud Chamber, Magnet and Cyclotron	20
3.	EXPERIMENTAL ARRANGEMENT	23
	A. Selection of the Target	23
	B. Collimation	23
	C. Alignment	26
	D. Operation of the Cloud Chamber	28
4.	REPROJECTION AND ANALYSIS OF THE PHOTOGRAPHS	29
	A. Reprojection of the Photographs	29
	B. List of Quantities Measured for Each Track	29
	C. List of Quantities Calculated for Each Track	31
	D. Acceptance Criteria	33
5.	RESULTS AND CONCLUSIONS	35
6.	MESON EVENTS	45
7.	EXPERIMENTAL CHECKS AND DISCUSSION OF ERRORS	49
8.	ACKNOWLEDGMENTS	58
REFERENCES		59
APPENDIX A		60
	1. Derivation of the Formula for the Error in the Energy of a Neutron	60
	2. Energy Resolution of the Cloud Chamber	62
	3. Operation of Unfolding Errors of Measurement from the Experimental Neutron Spectrum	63
	4. Loss of Neutrons through Lower Energy Boundary, Assuming Gaussian Errors of Measurement	65
	5. Loss of Neutrons through Lower Energy Boundary, Assuming Non-Gaussian Errors of Measurement	66

TABLE OF CONTENTS

	Page No.
APPENDIX B	
1. Derivation of Equations (2), (5) and (6) which Appear in the Text	69
APPENDIX C	72
Nomographs	72
1. Nomographs for Calculation of the Neutron Energy	72
Circular Nomographs	77

A HIGH-PRESSURE CLOUD-CHAMBER INVESTIGATION OF PROTONS SCATTERED BY 300 MEV NEUTRONS

John De Pangher, Jr.

Radiation Laboratory, Department of Physics
University of California, Berkeley, California

March 16, 1953

ABSTRACT

An investigation of the protons scattered by 300 Mev neutrons has been conducted with a Wilson cloud chamber filled with hydrogen at a gas pressure of ten atmospheres. The data obtained covers the range of angles 10° - 180° for the neutrons in the center of mass system. A striking deviation from theoretical predictions occurs for small neutron scatter angles. The energy spectrum is presented for the neutrons which are produced in a 1-3/4 in. thick Li D target by 340 Mev protons. A few cases of meson production are noted.

A HIGH-PRESSURE CLOUD-CHAMBER INVESTIGATION OF PROTONS SCATTERED BY 300 MEV NEUTRONS

John De Pangher, Jr.

Radiation Laboratory, Department of Physics
University of California, Berkeley, California

March 17, 1953

1. INTRODUCTION

A number of neutron-proton scattering experiments[1-6] with the energies of the incident neutrons ranging from 27 Mev to 260 Mev have been conducted during the past five years for the purpose of obtaining information about nuclear forces. A deviation from isotropic scattering in the center of mass system was observed[1] at Los Alamos with 27 Mev neutrons evolved in the d, t reaction. The first experimental evidence[2, 3] for the existence of exchange forces in n-p scattering was furnished by the data made available with 90 Mev neutrons produced in the "stripping" process at Berkeley. By employing neutrons generated in the proton bombardment of beryllium, workers at Harwell[4] (neutron energy 156 Mev), Rochester[5] (neutron energies 172 and 215 Mev), and Berkeley[6] (neutron energy 260 Mev) have furnished additional evidence for the exchange process.

With only one exception[3] the experimental procedure employed for the work just mentioned used counters. Counter telescopes, consisting of either scintillation crystals or proportional counters filled with gas, are inclined at an adjustable angle to the neutron beam to observe the recoil protons emerging from a target, for example, polyethylene, upon which the neutrons are incident. The experiment is repeated except that the polyethylene is replaced by carbon so that the number of events originating from the hydrogen in the polyethylene may be determined by subtraction. Absorbers are inserted in the telescope to select only those protons originating from neutrons of a definite band

of energy. Corrections are made for nuclear absorption and Coulomb scattering in the absorbers. Although the counter method is capable of yielding good statistical accuracy and energy resolution for a large range of proton deflection-angles, one experiences difficulty in using it to obtain information about protons scattered through large angles (or neutrons scattered through small angles in the center of mass system). For example, the smallest neutron angle attained in the 90 Mev case was 36.0°, while in the 260 Mev case it was 37.7°.

The cloud chamber, filled with hydrogen and located in a strong magnetic field, offers a simple independent method, relatively free from corrections, for investigating protons scattered by high energy neutrons. Low energy protons which end in the illuminated region of the cloud chamber ionize heavily and hence are very conspicuous. Even for the high pressure (104 psig in expanded position) cloud chamber to be described later in this paper, a proton with an energy as low as 1.09 Mev has the easily measurable range of 1.4 cm. Bruechner[3] et al., employing a cloud chamber in a magnetic field, measured the angles and curvatures of the knock-on protons produced by 90 Mev neutrons in hydrogen. Neutrons whose angles were as small as 12° (center of mass system) were included in their data.

Phenomenological descriptions of the n-p interaction in terms of a static potential have been given by a number of investigators. Only a few[7,8,9] will be referred to in this paper. A summary of the comparison between theory and the angular distribution data[2,6] obtained at Berkeley is given by Chamberlain[10] et al. The theory of Christian and Hart predicts a differential cross section which is symmetrical about 90° in the center of mass system, but the theory of Christian and Noyes and the theory of Jastrow do not exhibit this symmetry property. However, they essentially agree on one feature; namely, that the cross section reaches approximately the same high value at 0° as it does for 180°. The high energy measurements (260 Mev neutrons) of Kelly[6] et al. do not extend far enough into small neutron angles to verify this point.

It is the object of this experiment to verify by an independent method the experimental data of Kelly et al., and to extend that data into small neutron angles. A Wilson cloud chamber, filled with hydrogen and operating at ten atmospheres gas pressure was designed for this experiment.

The cloud chamber method also presents the possibility of observing directly mesons produced by high energy neutrons in hydrogen. The threshold energy for the reaction $n + p \rightarrow \pi^0 + d$ is 274 Mev, while it is 292 Mev for the two other expected reactions: $n + p \rightarrow \pi^+ + n + n$ and $n + p \rightarrow \pi^- + p + p$. However, the cross sections for these reactions are small, so only a very few mesons were found in the course of the experiment.

2. THE TEN-ATMOSPHERE WILSON CLOUD CHAMBER

A. General Features of Construction

Some of the advantages of a high-pressure cloud chamber over one that operates near atmospheric pressure are: (1) the tracks are sharper, (2) the sensitive time is longer, (3) the tracks are rendered more visible because of greater ionization density, and (4) there is a greater density of target nuclei for the incident radiation. A disadvantage which partially offsets (4) in the rate of accumulation of data is that a longer time is required for the gas to become resaturated with water vapor after removal of the drops and to reach thermal equilibrium.

With these points in mind, a ten-atmosphere cloud chamber, with thin windows to admit the neutron beam from the cyclotron, was constructed to fit in the six-inch gap of a magnet[12] which provides a field of 21,700 gauss in pulsed operation. In the expanded position of the chamber a cylindrical volume twelve in. in diameter and three in. high is available for the production of tracks. Of this space, a region 10.5 in. in diameter and 2.5 in. high is uniformly illuminated for photography.

Figure 1 shows a photograph of the cloud chamber (1) with expansion boxes (2). Each expansion box contains a quick-acting valve which is remotely controlled by the magnetic pullers (3) through a length of piano wire (4). When the cloud chamber is put into the magnet for use with the cyclotron, the pullers are located just outside the fringing field of the magnet. Air cylinders (5) serve to reset the magnetic pullers following an expansion. The tension in the piano wire is adjusted by means of the adjusting screw (6) which serves to slide the puller along the base (7) on which it is mounted.

The main features of the chamber will now be discussed with the aid of Figs. 2A and 2B, which employ a common numbering system. Fig. 2A displays a drawing of the chamber while Fig. 2B shows an enlargement of a portion of Fig. 2A for the purpose of discussing the thin-window structure.

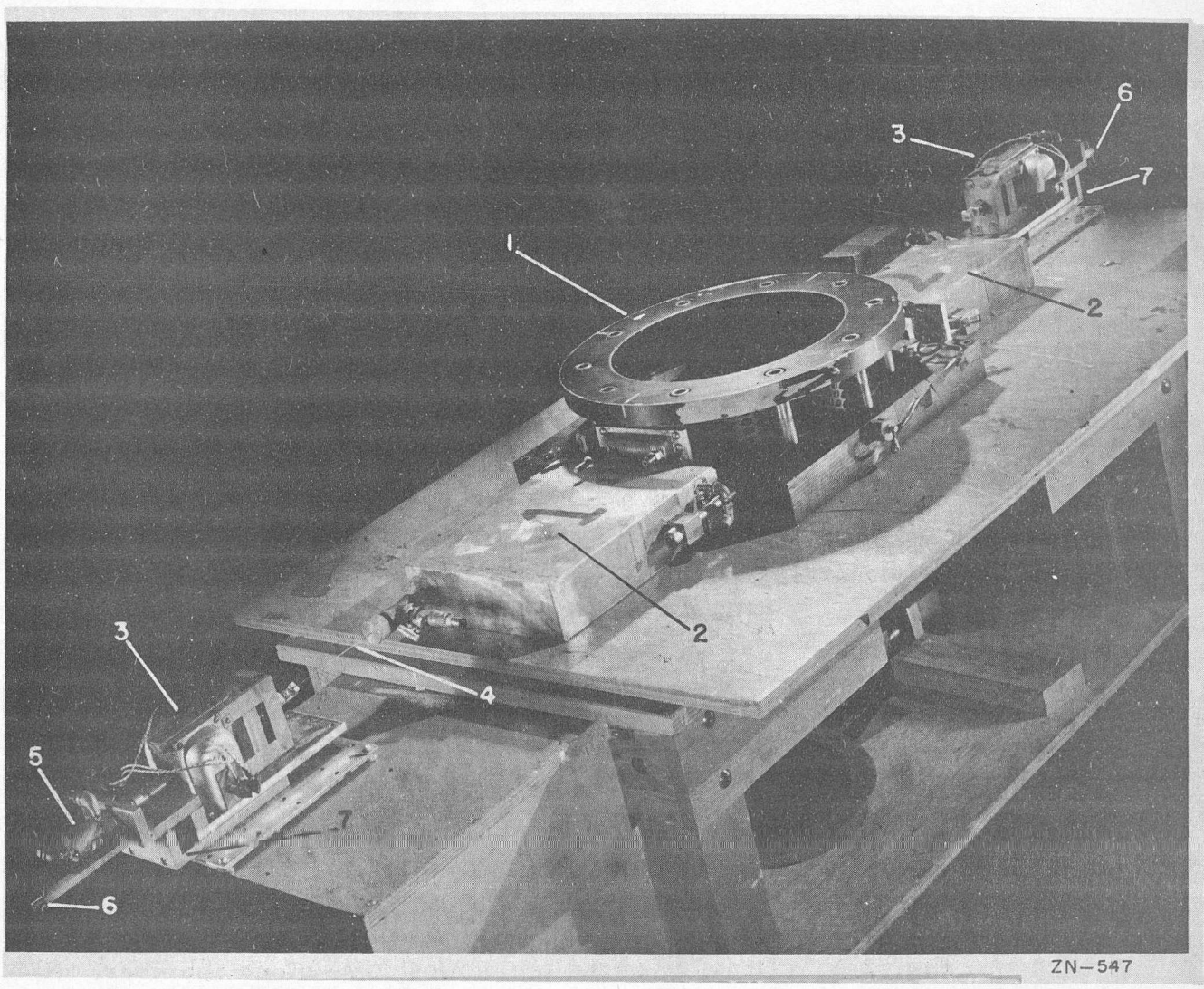

Fig. 1 Photograph of the ten-atmosphere cloud chamber assembled with expansion boxes and magnetic pullers. (1) cloud chamber, (2) expansion boxes, (3) magnetic pullers, (4) piano wire, (5) air cylinders, (6) adjusting screw, and (7) base of the puller.

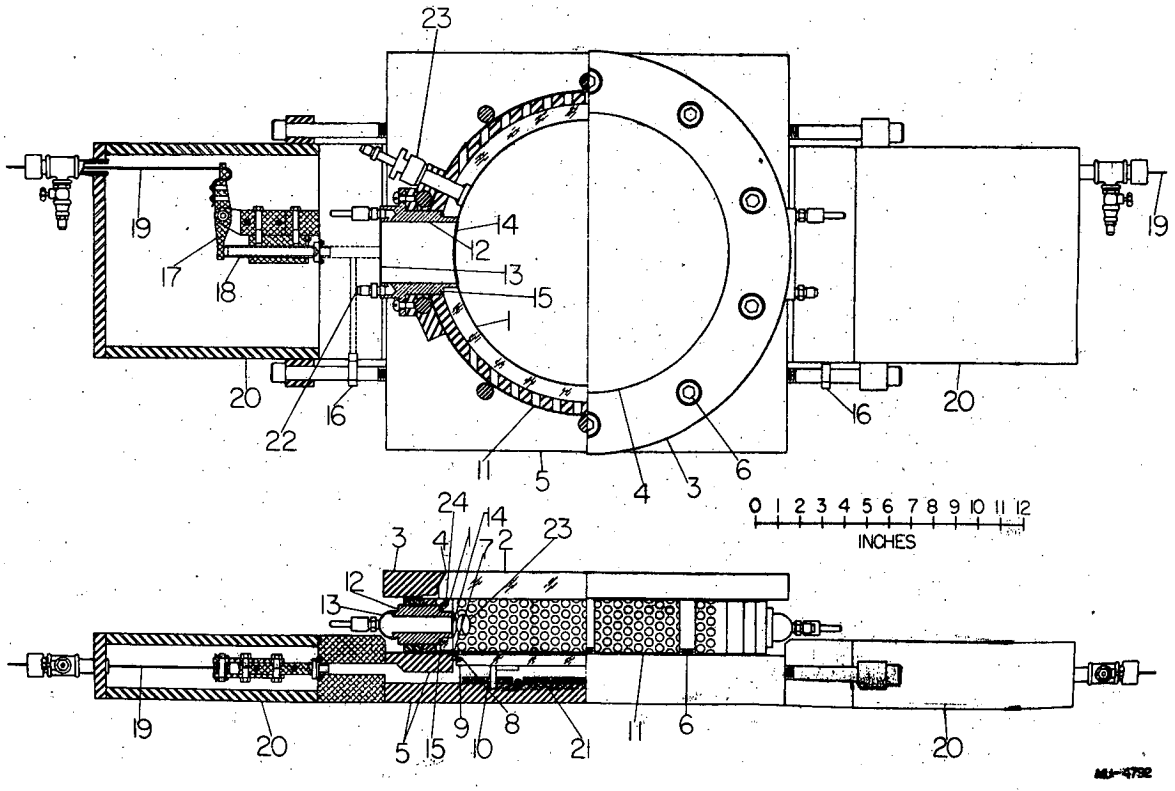

Fig. 2 A Drawing of the ten-atmosphere cloud chamber. (1) Lucite ring, (2) cover glass, (3) stainless steel clamping ring, (4) Wood's metal gasket, (5) cloud chamber base, (6) stainless steel clamping bolts, (7) rubber diaphragm, (8) second sheet of rubber, (9) Lucite disk, (10) equalizer arm, (11) perforated stainless steel ring, (12) brass window frame, (13) outer Be-Cu foil, (14) inner Be-Cu foil, (15) "0" ring, sealing at the brass window frame, (16) inlet or outlet to lower volume of cloud chamber, (17) expansion-valve lever, (18) expansion-valve piston, (19) piano wire, (20) expansion box, (21) neoprene pad, (22) gas inlet to window, (23) filling valve or inlet to upper volume of cloud chamber and (24) "0" ring, sealing at the cover glass.

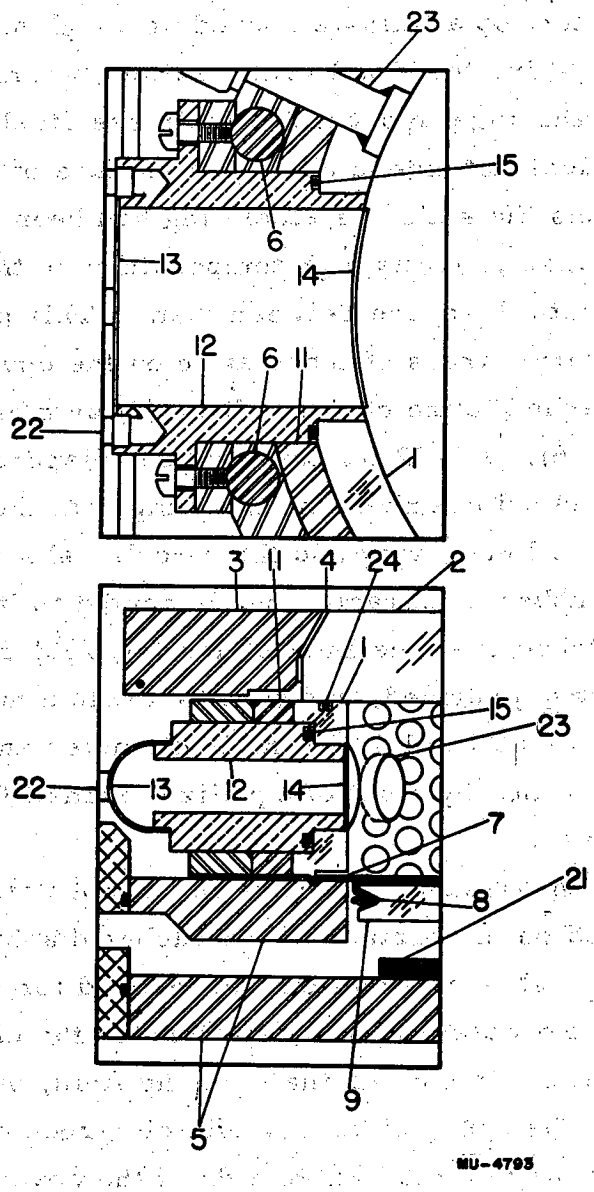

Fig. 2 B An enlargement of a portion of Fig. 2 A for the purpose of showing the thin-window structure. See Fig. 2 A for key to numbers shown above.

The central part of the cloud chamber consists of a twelve in. diameter Lucite ring (1) 2-1/2 in. high and 3/4 in. thick. There is located on the top a fully-tempered cover glass (2) (trade name Herculite), 1-1/4 in. thick and with maximum diameter 13-1/4 in. It is beveled at the edge to set into a stainless steel clamping ring (3) so that the latter does not extend above the surface of the glass. Previously, the glass and the stainless steel ring had been assembled and placed in an oven at a sufficiently high temperature so that Wood's metal (4) could be poured into the space between them. This procedure was adopted to insure uniform stress concentration on the cover glass when the clamping ring is attached to the chamber base (5) by means of ten 3/4 in. stainless steel bolts (6). A 1/32 in. thick rubber diaphragm (7) extends horizontally across the cloud chamber and is clamped at the edge between the ridged bottom of the Lucité ring and the circular slot in the chamber base. Beneath the rubber diaphragm, and cemented to it, a second sheet of rubber (8) is stretched over the Lucite disk (9), folded over its edge into the "V"-shaped groove provided, and then tied with a number of layers of fish line. The Lucite disk (9), 11-13/16 in. in diameter and 1/2 in. thick is maintained level at all times by a set of equalizer arms (10) which are fastened to the chamber base.

A preparation consisting of hot water, gelatin and black dye when poured on the surface of the rubber diaphragm soon cools and solidifies and furnishes an excellent background for photography. In addition, it supplies the water vapor that saturates the cloud chamber, and serves as the lower electrode for the clearing field, when maintained at ground potential. The upper clearing-field electrode consists of a ring of aquadag which is painted on the bottom side of the cover glass. A small amount of soap when rubbed on the cover glass with the fingers and then polished with cotton permits a thin invisible layer of water to condense on the glass, thus rendering it conducting. A thin copper foil inserted between the cover glass and the Lucite ring allows an electrical connection to be made with the aquadag layer from the outside.

To enable the 3/4 in. thick Lucite ring (1) to withstand a gas pressure of ten atmospheres, it was enclosed by a close-fitting stainless steel ring (11) 9/16 in. thick. A series of holes was drilled in the stainless steel so that the light emanating from two flash lamps situated on opposite sides of the chamber could illuminate the active volume in which tracks are formed. After a series of illumination tests had been made with wooden models of the steel ring, a perforation pattern with fifty percent transparency was selected. This choice represented a suitable compromise between the requirements of structural strength and uniform illumination. Although the Lucite ring could have been made stronger by increasing its thickness, the need for windows of maximum possible area always led to a design in which the Lucite ring alone was structurally inadequate.

Up to 12.5 cm^2 of neutron beam may be admitted through thin windows into the cloud chamber. On the side of the chamber where the neutron beam is to be introduced, a detachable thin-window unit, consisting of a hollow brass frame (12) with thin curved foils (13, 14) of beryllium copper alloy hard-soldered to its extremities, penetrates the stainless steel (11) and the Lucite rings (1). The outer foil (13), 0.003 in. thick, is bent into a half-cylinder of diameter 1.25 in., while the inner foil (14), 0.005 in. thick is shaped to follow the contour of the inner surface of the Lucite ring. An "0" ring (15) rests in a groove in the brass frame and touches the outer surface of the Lucite ring. Six machine screws which screw into the stainless steel ring (11) force the brass frame (12) against the Lucite so that the "0" ring is compressed to give a pressure seal. In order to reduce the strain on the inner foil (14) (less curved than the outer one) when the cloud chamber is filled with gas at high pressure, gas is introduced into the window cavity and maintained there at a pressure slightly lower than the minimum pressure inside the cloud chamber immediately after an expansion occurs. A second thin-window unit, identical to the one just described, is located on the opposite side of the cloud chamber for the purpose of reducing back-scattering of neutrons.

Gas at regulated pressure is introduced through an inlet (16) into the cloud chamber base (5) to control the expansion ratio. As mentioned previously, two magnetic pullers control symmetrically-located expansion valves (17, 18) by means of two lengths of taut piano wire (19), 0.029 in. thick, which pass through small holes in the ends of the expansion boxes (20). During an expansion of the cloud chamber the valves are opened simultaneously to let the gas rush into the expansion boxes while neoprene pads (21) stop the downward motion of the Lucite disk.

B. The Gas Control System

The gas control system will now be described by referring to Fig. 3. Hydrogen gas, leaving the high-pressure tank (1), passes through a pressure regulator (2), enters the liquid air trap (3), moves through a filter (4) and finally is admitted through a filling valve (5) into the upper volume (6) of the cloud chamber at a pressure p_{uv}. A vacuum system is not necessary to remove the original gas contained in the upper volume since it is simpler to flush the upper volume a number of times with the aid of the bleed valve (7) until the desired purity of hydrogen is obtained. A precision Bourdon gauge (8), calibrated to an accuracy of ± 0.25 percent, is provided to measure the pressure p_{uv}.

Helium gas, leaving the high pressure tank (9), passes through a pressure regulator (10), enters the window cavities (11) and is maintained at a pressure p_w.

The high pressure system which controls the expansion ratio of the cloud chamber may be described as follows. Five nitrogen tanks (12) (gas pressure 2300 psi when full) are connected through a manifold (13) to a pressure regulator (14). Nitrogen at a pressure 200 psi is stored in the tank (15) which is heated to partly compensate for the cooling of the gas in falling through the large pressure differential. The storage tank (15) contains a large enough volume of nitrogen to sustain a few expansions of the cloud chamber when the tanks (12) become empty and are replaced by full ones. The nitrogen now flows through the precision pressure

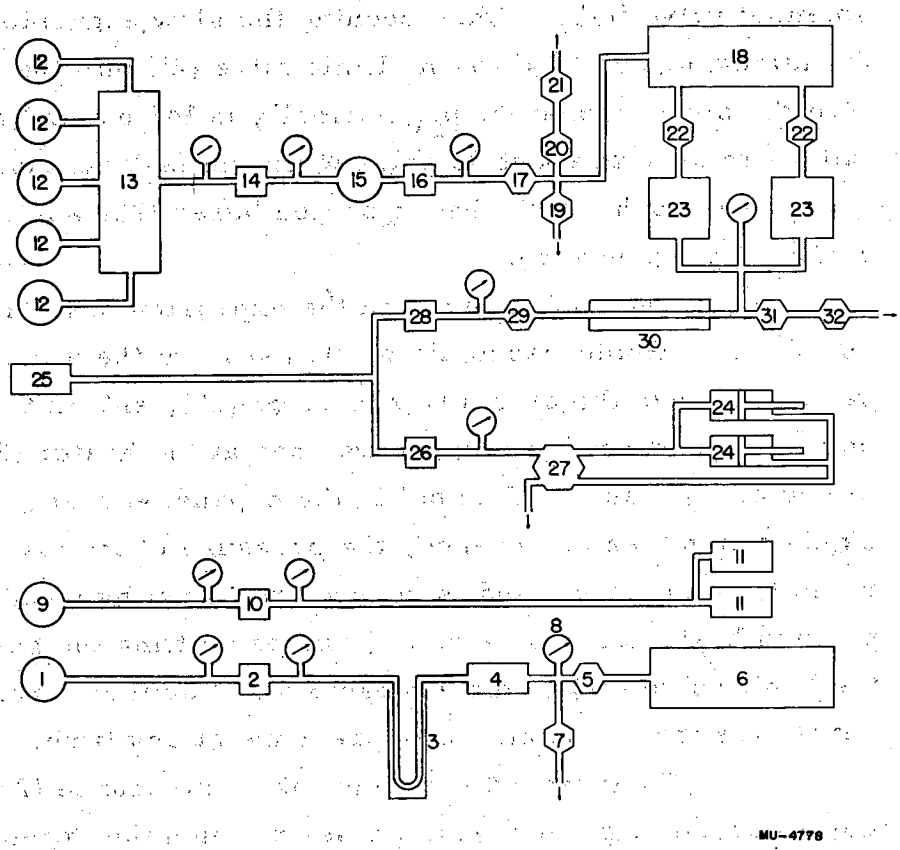

Fig. 3 Gas control system. (1) hydrogen tank, (2) pressure regulator, (3) liquid air trap, (4) filter, (5) filling valve, (6) upper volume of cloud chamber, (7) bleed valve, (8) precision pressure gauge, (9) helium tank, (10) pressure regulator, (11) window cavities, (12) nitrogen tanks, (13) manifold, (14) pressure regulator, (15) storage tank with heater, (16) precision pressure regulator, (17) "fill lower volume" solenoid valve, (18) lower volume of cloud chamber, (19) safety valve, (20) slow expansion valve, (21) limit valve, (22) fast expansion valves, (23) expansion boxes, (24) air cylinders, (25) air compressor, (26) pressure regulator, (27) "pneumatic reset" solenoid valve, (28) pressure regulator, (29) "fill expansion boxes" solenoid valve, (30) heater, (31) "dump expansion box" solenoid valve and (32) limit valve.

regulator* (16) to the "fill lower volume" solenoid valve (17) and then onward to the space beneath the rubber diaphragm which shall henceforth be called the lower volume (18) of the cloud chamber. Let $p_{\ell v}$ denote the pressure of gas in the lower volume. A safety valve (19) is provided. Slow expansions are achieved by first closing the "fill lower volume" solenoid valve (17) and then opening the slow expansion valve (20) to let the nitrogen pass through the limit valve (21) into the atmosphere. Before the slow expansion, $p_{\ell v}$ normally is 148 psi and the limit valve permits it to drop to about 93 psi. When the fast expansion valves (22) are opened gas rushes into the expansion boxes (23) which contain compressed air at 20 psi pressure.

The gas controls on the expansion boxes may be described as follows. Compressed air at 100 psi from the air compressor (25) passes through the pressure regulator (28), enters the "fill expansion boxes" solenoid valve (29), is warmed at the heater (30) and is maintained at a pressure of 20 psi in the expansion boxes (23). When the expansion valves are opened, the pressure of the air-nitrogen mixture rises to about 78 psi and is reduced to 20 psi by opening the "dump expansion box" solenoid valve (31) and permitting the gas to flow through the limit valve (32) to the atmosphere. For future reference, let p_{eb} denote the air or air-nitrogen pressure at any time.

Compressed air from the same source (25) emerges from the pressure regulator (26), passes through the "pneumatic reset" solenoid valve (27) to the air cylinders (24) which reset the magnetic pullers just after an expansion of the chamber is completed.

Table 1 shows some typical pressures (psig) attained in operating the cloud chamber with hydrogen as the filling gas.

---

* Moore Products Co. Model 200.

TABLE 1

Operation	p_{uv}	$p_{\ell v}$	p_w	p_{eb}
flushing	5-50-5	0	0	0
filling	0-106	0-93	0-93	0
expansion	147-93-106	148-78	93	20-78

p_{uv} = hydrogen pressure in the upper volume
$p_{\ell v}$ = nitrogen pressure in the lower volume
p_w = helium pressure in the window cavities
p_{eb} = pressure of the air or air-nitrogen mixture in the expansion boxes

Fig. 4 displays a typical cycle of operation for the key valves in the gas control system which has just been described. The time between successive fast expansions of the cloud chamber is two minutes.

C. Photography

A specially constructed camera is mounted on a light-tight crown 27.5 in. above the cover glass. Pictures are taken through a pair of Leica Summitar 50-mm. lenses at f5.6 on Eastman Linagraph Ortho film in 100 foot strips 1.80 in. wide. Two G.E. FT-422 flash-tubes are mounted in light-tight boxes on the sides of the cloud chamber. Two condenser banks, each of capacity 256 μf. and charged to 1500 volts, constitute the energy source for the glash-tubes. Light from them, having been rendered parallel by cylindrical lenses made of Lucite, passes through the perforated stainless steel wall of the cloud chamber to the interior. A third lens on the camera is used to view a number counter for the identification of each picture, and to view an ammeter (see later section on the magnet) which measures the current flowing through the magnet.

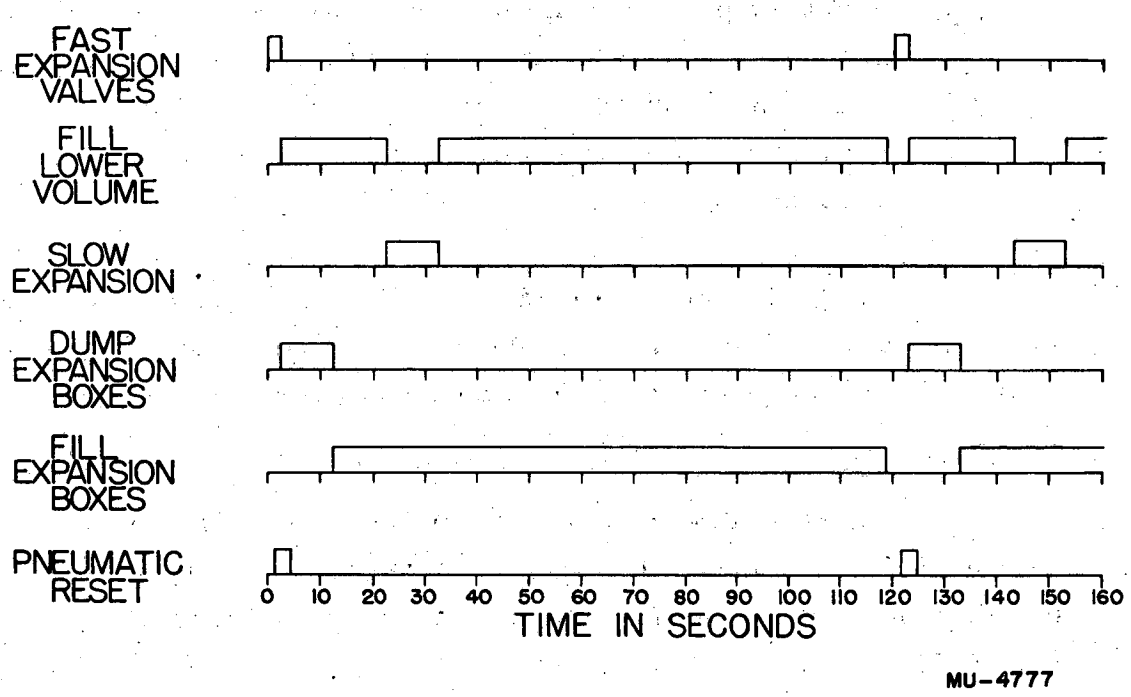

Fig. 4 Typical cycle of operation of the electrically-operated valves in the gas control system.

D. Magnet

The cloud chamber is operated in a magnet[12], which, when energized and pulsed with a current of 4000 amperes supplied by a 150 h.p. mine-sweeper generator with a five-ton flywheel, furnishes a magnetic field strength of about 21,700 gauss. The maximum variation of the magnetic field over the volume of the chamber in which tracks are photographed does not exceed 2.5 percent. A table constructed from a uniformity plot of the magnetic field enables one to determine the field strength at the center of each track measured to an accuracy of ± 0.5 percent. A large ammeter, used in the calibration of the magnetic field, and permanently mounted on the magnet-control cabinet, is read to an accuracy of ± 0.25 percent each time the magnet is emergized. Although one tries to maintain the magnet current at 4000 amperes, occasionally a drift of a few amperes may occur, and so a small correction on the magnetic field is made for this deviation. In case a reading of the large ammeter is missed, one depends on the reading of a smaller ammeter which is recorded on each picture to obtain the magnet current.

E. Temperature Control

The main body of the cloud chamber is maintained at a temperature of 19° C by a temperature-controlled water circulating system in the gap of the magnet. To avoid the development of a temperature gradient inside the cloud chamber from gas flow into the lower volume of the chamber, from discharge into the expansion boxes, and from subsequent exhaust into the atmosphere, the gas is pre-heated (See mention of heaters in the section on the gas control system.) before it reaches the chamber. A bridge-circuit employing Western Electric thermistors as resistance elements, and a Leeds and Northrup Micromax Recorder, ten millivolts full scale, records the temperature difference between the top and bottom of the chamber. In the course of a long run the bottom becomes colder than the top, but the temperature control is adequate to keep the temperature difference below 0.5° C (about 0.5 millivolts deflection on the recorder).

F. Synchronization of Cloud Chamber, Magnet and Cyclotron

The timing system consists of,(1) a slow timer, (2) a fast timer and, (3) an oscilloscope for measuring time intervals.

The slow timer controls the solenoid valves in the gas control system that perform the following operations: (1) fill lower volume, (2) slow expansions, (3) fill expansion boxes, (4) dump expansion boxes and, (5) pneumatic reset. The valves are either manually controlled by toggle switches, or are automatically operated by microswitches which rest on cams driven by a variable speed d. c. motor. In addition, the slow timer activates the film-wind mechanism, turns on the magnetic field, and operates a time delay which, in turn, triggers the fast timer.

Vacuum-tube-operated relays in the fast timer perform such operations as, (1) shorting out the clearing field just before an expansion of the cloud chamber, (2) flashing lights which illuminate the number-counter and the magnetic field current meter, (3) starting the fast expansion, (4) pulsing the cyclotron and, (5) initiating the condenser discharge through the flash-tubes. An adjustable RC-network in the grid circuit of each vacuum tube (6SN7) allows a time-range-control up to 200 milliseconds.

It takes about 2. 5 seconds for the magnet current to reach the value 4000 amperes, where it remains steady for about 0. 2 second before being turned off. The time delay on the slow timer is adjusted so that the fast expansion is completed during the steady period of the magnet current. A few milliseconds later the cyclotron is pulsed three times and the neutrons pass through the cloud chamber.

Fifty milliseconds after the third pulse of neutrons has entered the chamber the lights are flashed. In this way, pictures of proton-recoil tracks produced in hydrogen are very sharp and practically free from turbulence.

One views timing signals from the rapid succession of events just described on an oscilloscope with a persistent screen. The horizontal time sweep is triggered at the instant the slow timer starts the fast timer. Timing marks for calibration of the horizontal sweep are spaced 1/60 sec. apart. The following signals, after passing through a pulse-shaping circuit, appear on the vertical sweep: (1) signals from the relays in the fast timer which initiate the fast expansion and the condenser discharge through the flash-tubes, (2) a signal from a switch called the bottom switch in the chamber base (This switch is closed when the expansion is completed.) and, (3) signals from a counter responding to the cyclotron pulses. Fig. 5 shows graphically the succession of events which occur when the cloud chamber is operated with the cyclotron.

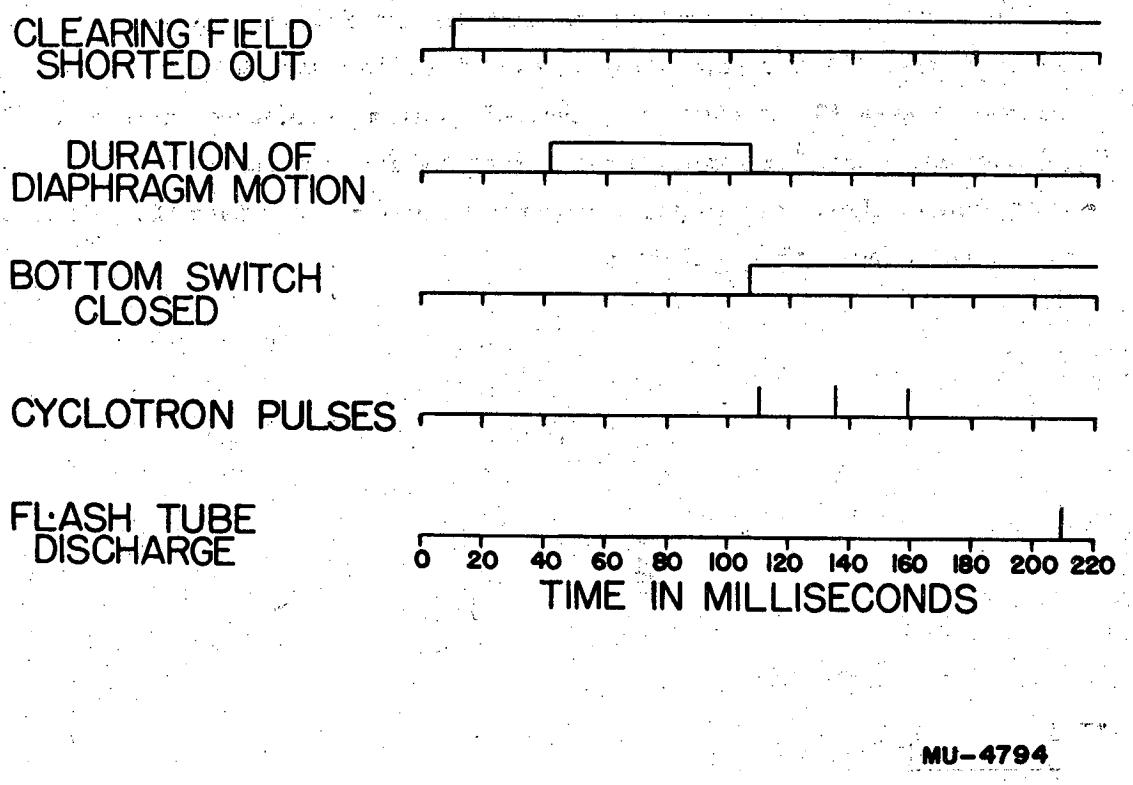

Fig. 5 Succession of events occurring when the cloud chamber is operated with the cyclotron.

3. EXPERIMENTAL ARRANGEMENT

A. Selection of the Target

Figure 6 shows the results of some work by W. P. Ball[11] and W. Hess on the comparison of the effectiveness of (1) a two in. thick beryllium target and (2) a 1/2 in. thick lithium-deuteride target for the production of high energy neutrons in the 340 Mev proton beam of the Berkeley cyclotron. Although (1) gives a greater yield of neutrons than does (2), (2) gives a narrower spectrum and a proportionally smaller low energy tail. If a thicker lithium-deuteride target were employed, one might hope for a higher yield of neutrons without sacrificing too much of the desirable features of the thinner target. A brief experiment with the high pressure cloud chamber, filled with hydrogen, revealed the fact that just as many neutrons with energies above 200 Mev were produced by a 1-3/4 in. thick lithium-deuteride target* as from the 2 in. thick beryllium target. There were much fewer neutrons of lower energies however. Accordingly, the 1-3/4 in. thick lithium-deuteride target was used in the n-p scattering experiments which are about to be described in this paper.

B. Collimation

See Fig. 7 for a sketch of the collimating system. The neutron beam from the cyclotron passes through circular holes in the tapered lead collimator and the concrete shielding, through rectangular holes in the first and second copper collimators, and finally through the thin windows of the cloud chamber. Table 2 gives some data on the dimensions of the components of the collimating system.

---

* Supplied by W. P. Ball.

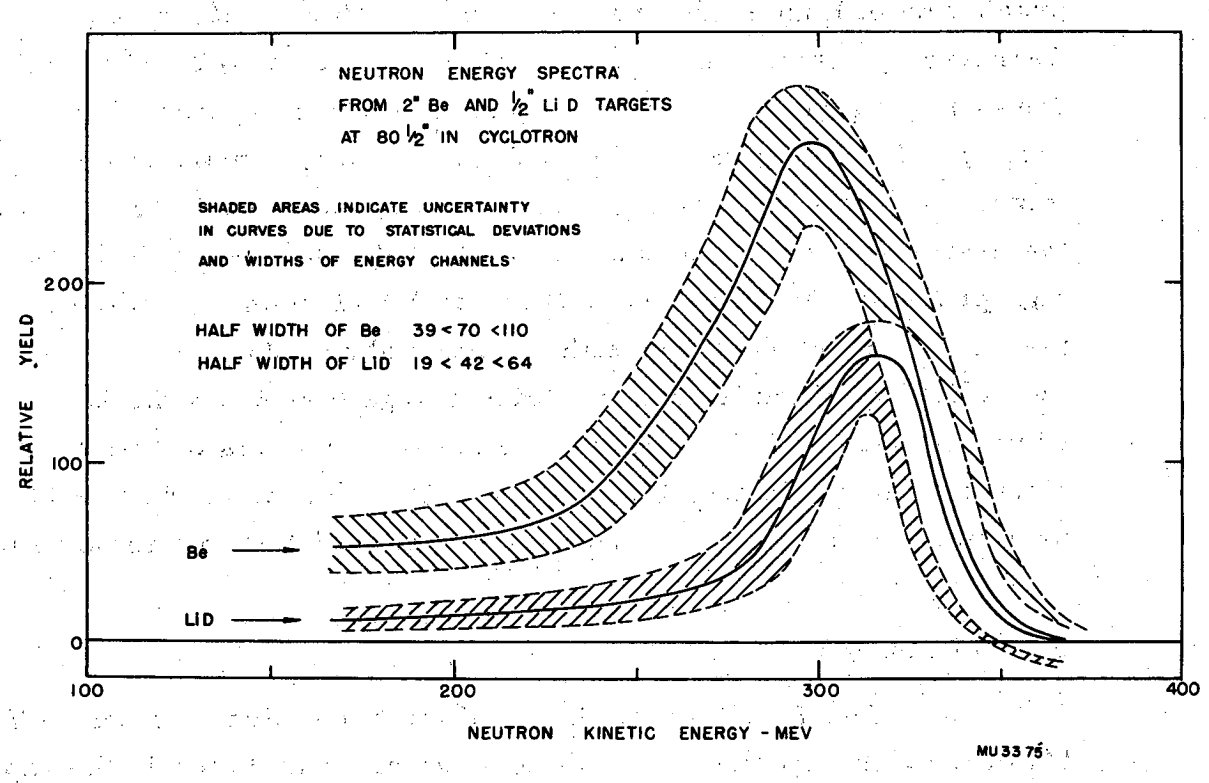

Fig. 6 Energy spectrum of neutrons from a Li D target 1/2 in. thick. The results shown are due to Ball[11] and Hess.

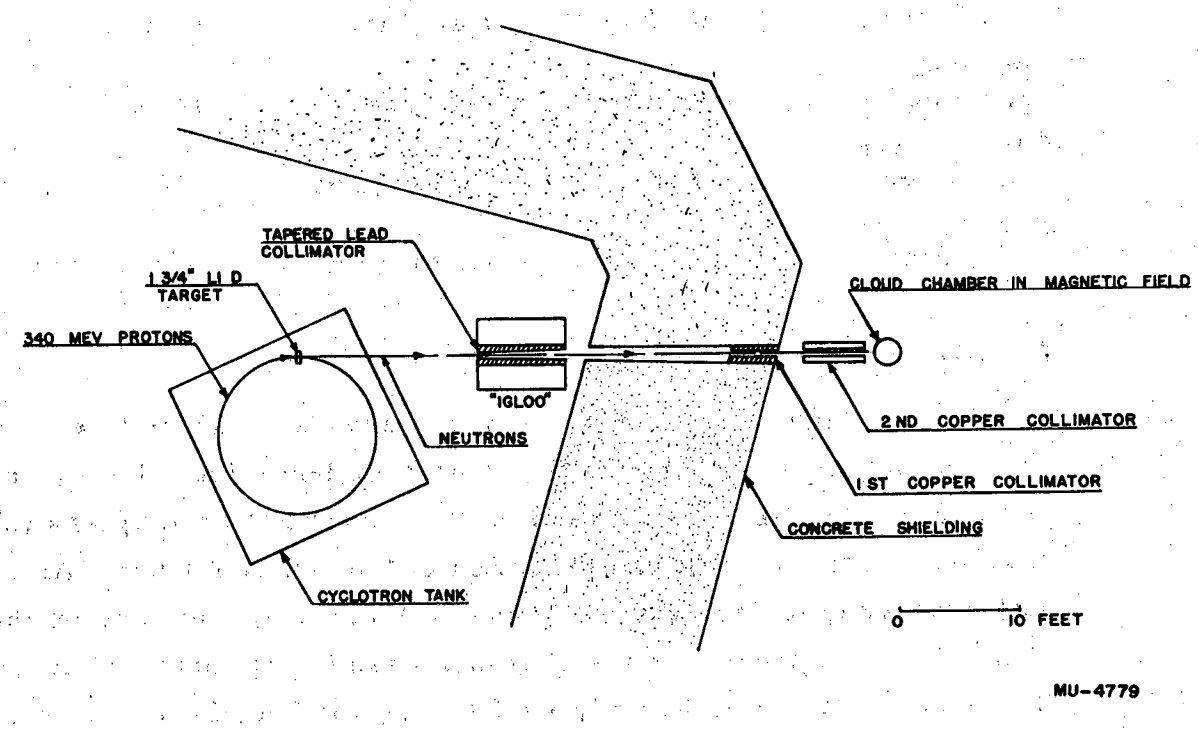

Fig. 7 Collimating system.

TABLE 2

Dimensons on the components of the collimating system.

Component	Length	Shape of Hole	Dimensions of Hole
tapered lead collimator	86.5 in.	circular	6 in.
concrete shielding	208.0 in.	circular	12 in.
first copper collimator	30.0 in.	rectangular	1/2 in. x 2 in.
second copper collimator	34.0 in.	rectangular	5/8 in. x 2-1/4 in.

C. Alignment

Figure 8 shows some of the apparatus which is employed for aligning the cloud chamber with the neutron beam from the cyclotron. A set of five crosses (1) is marked on the horizontal cover glass (2) of the cloud chamber to define the direction of the neutron beam. An auxiliary unit consisting of two sets of ~~crosses (3) which are scribed on the Lucite~~ plates (4) is attachable to the chamber base (5) by means of the rigid arm (6). The auxiliary unit is adjusted so that the line defined by the crosses in it passes through the center of the chamber directly below and parallel to the line defined by the crosses on the cover glass. After the cloud chamber and auxiliary unit have been placed in the magnet, the second copper collimator (7) (See also Fig. 7) is aligned with the system just described and then it is bolted to a platform on the magnet frame. The magnet is rotated, translated, or tilted by means of an overhead crane until an observer with telescope (9) near and in line with the target (8) in the cyclotron sees the crosses coincide. In this way, the cloud chamber is aligned with the direction of the neutron beam to an accuracy of ± 0.25 degrees.

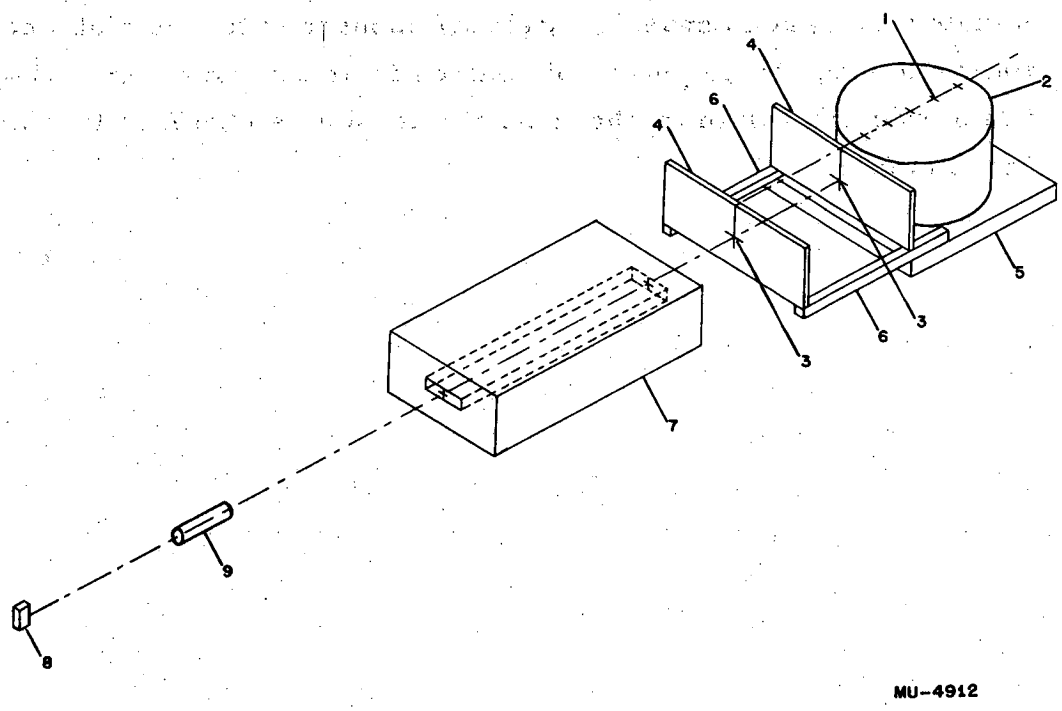

Fig. 8 Alignment system. (1) five crosses, (2) cover glass of cloud chamber, (3) crosses, (4) Lucite plates, (5) chamber base, (6) rigid arms, (7) second copper collimator, (8) target inside cyclotron tank, (9) telescope.

D. Operation of the Cloud Chamber

The manner in which the cloud chamber and magnet are synchronized with the cyclotron has already been described in Section 2F. Nearly all the data which will be presented here was taken in two runs, each lasting two days. The time between expansions was two minutes with each expansion yielding about four to five high energy proton recoils for three pulses of neutron from the cyclotron. One picture in ten was taken without the magnetic field as a check on turbulence in the chamber.

4. REPROJECTION AND ANALYSIS OF THE PHOTOGRAPHS

A. Reprojection of the Photographs

A double projector, Fig. 9, employing two Western Union arc lamps, type 100, throws a pair of life-size images of the tracks formed in the cloud chamber on a special coated glass plate (Eastman Recordak green translucent screen). The focus of each lens in the projector is adjusted and the film is moved in its holder until the images of the five crosses on the cover glass of the cloud chamber become normal size and coincident. The zero setting for the beam angle β (angle of rotation about a vertical axis) is made while the line BB on the measuring plate lies along the superimposed images of the five crosses. The dip angle α (angle between the measuring plate and a horizontal plane) is also zero when the measuring plate is in the position just described.

B. List of Quantities Measured for Each Track

The following quantities were measured or recorded for each track:

1. The slant radius of curvature ρ_s (cm.), or range R (cm.) if the track ends in the illu-- minated part of the chamber.
2. The dip angle α (degrees).
3. The beam angle β (degrees).
4. The distance Z_o (in.) from the bottom of the cover glass to the origin of the track.
5. The length L (cm.) of the chord of the track.
6. The distance Z_m (in.) from the bottom of the cover glass to the center of the track.
7. The radial distance r (in.) from the center of the track to the center of the chamber.

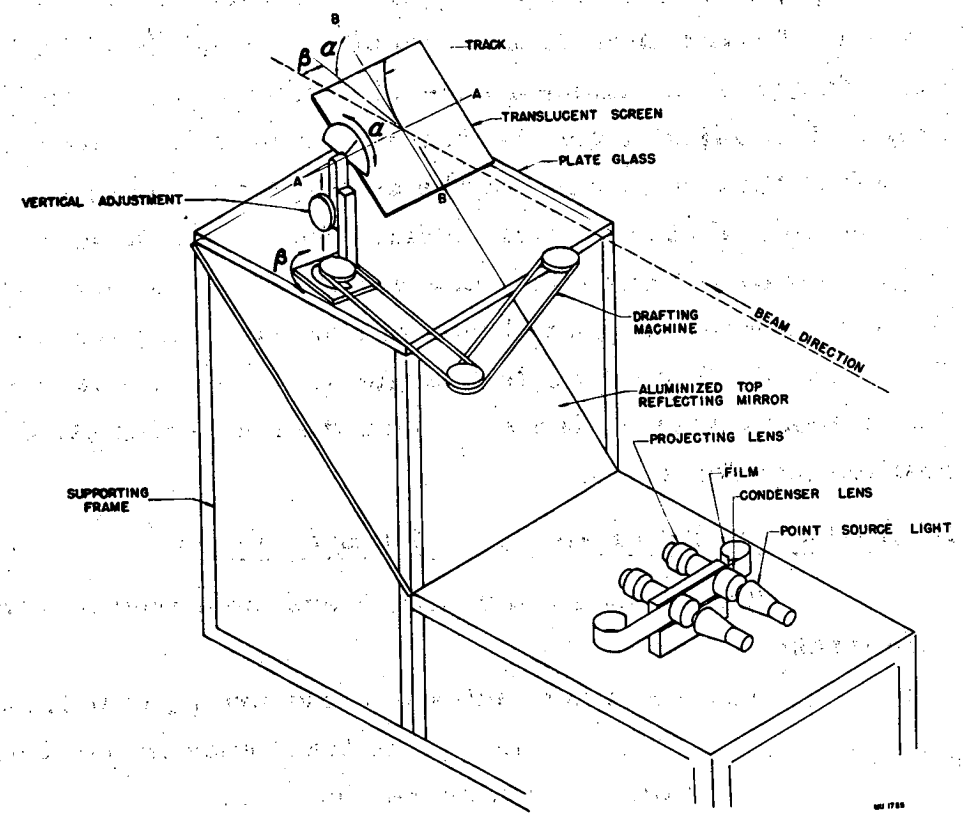

Fig. 9 Reprojection apparatus.

8. The magnet current I (amperes) as read on the large ammeter on the magnet platform (See section 2D).
9. The magnet current I' as read on a small ammeter which is photographed (See section 2D).
10. The counter number to identify a stereoscopic pair of pictures.

A vertical adjustment and translation of the measuring plate, Fig. 9, still in a horizontal position, is made until the origin of the track appears on the horizontal axis AA of rotation. The plate is rotated about the vertical axis until the line BB is approximately parallel to the track and then is rotated through the dip angle α about the horizontal axis until the two track images coincide. The slant radius of curvature ρ_s is measured by matching it to one of a series of arcs ruled on a Lucite template. During this process another adjustment is made in which a single line on the Lucite template perpendicular to all the arcs is matched to the line AA to insure an accurate determination of the beam angle β. The quantity Z_o is measured to make sure that the track starts in the collimated region of the chamber. The quantities Z_m, r and I are used in the determination of the magnetic field strength B at the center of a track. The length of the chord of the track is measured so that the error in the measurement of ρ_s may be determined (See Appendix A1).

C. <u>List of Quantities Calculated for Each Track.</u>

1. $B\rho_s \cos \alpha$.
2. The kinetic energy T_p (Mev) of the proton.
3. The angle θ which the proton makes with the direction of the neutron beam.
4. The kinetic energy T_n (Mev) of the neutron which scattered the proton.
5. The angle θ' which the neutron makes with the direction of the neutron beam in the center of mass system.

6. The azimuthal angle ϕ.
7. The correction factor $f(\theta, \alpha_o)$, based on the assumption of azimuthal symmetry, where α_o is maximum dip angle accepted in reading tracks.

The quantities listed above are calculated from the following formulae:

$$B\rho_s \cos \alpha = \frac{10^4}{3} \left[T_p (T_p + 1876) \right]^{1/2} \tag{1}$$

$$\cos \theta = \cos \alpha \cos \beta \tag{2}$$

$$T_p = \frac{T_n \cos^2 \theta}{1 + T_n \sin^2 \theta/1876} \tag{3}$$

$$\tan \theta = \frac{\cot \theta'/2}{(1 + T_n/1876)^{1/2}} \tag{4}$$

$$\tan \phi \sin \beta = \tan \alpha \tag{5}$$

$$f(\theta, \alpha_o) = \frac{\pi/2}{\sin^{-1} \sin \alpha_o / \sin \theta} \tag{6}$$

Since the formulae (1), (3) and (4) appear frequently in the literature on n-p scattering their derivation will not be given here. However, derivation of formulae (2), (5) and (6) will be presented in Appendix B to this paper. Nomographs have been constructed for formulae (1), (3), (4) and (5) (See Appendix C) and have been used extensively throughout the calculations. The range-energy relationship for the high pressure hydrogen gas contained in the cloud chamber is shown on the nomograph for formulae (3) and is calculated from the tables of Aron, Hoffman and Williams.[13]

D. Acceptance Criteria

a. Lower Limit of 155 Mev on the Neutron Energy. The slant radius of curvature ρ_s of a proton recoiling from a neutron of energy T_n in a magnetic field B is given by the expression

$$\rho_s = \frac{\rho \cos \beta}{1 + T_n/1876 \sin^2 \theta} \tag{7}$$

where $$\rho = \frac{10^4}{3B} \left[T_n (T_n + 1876)\right]^{1/2} \tag{8}$$

and $$\cos \theta = \cos \alpha \cos \beta$$

The derivation of (7) and (8) which follows from (1) and (3) is simple so it will not be given here. By assuming the values B = 21,700 gauss and T_n = 155 Mev, one can calculate for $\alpha = 0^o$

$$\rho_s = \frac{86.2 \cos \beta}{1 + 0.1083 \sin^2 \beta} \tag{7'}$$

and for $\alpha = 50^o$

$$\rho_s = \frac{86.2 \cos \beta}{1.049 + 0.034 \sin^2 \beta} \tag{7''}$$

Unless the slant radius of a track is greater than the values indicated by formulae (7') and (7'') the track is rejected from further consideration.

b. Acceptable Region of the Cloud Chamber. A definite region of the cloud chamber from which tracks are acceptable was chosen for each of the two runs. For run No. 1, the dimensions of the region were 0.7 in. x 2.3 in. x 5.6 in. and for run No. 2 they were 0.7 in. x 2.3 in. x 6.7 in. The region selected for run No. 1 is smaller than it is for run No. 2 because of presence of the greater background of tracks from the window structure and collimators in run No. 1 than in the case of run No. 2.

c. Dip Angle Limitation. On account of the relatively small height of the active volume of the cloud chamber, tracks dipping steeply in the chamber become shorter with increasing dip angle. For example, the length of a proton track having a dip angle of fifty degrees may be as short as four cm. The uncertainty in the curvature measurement on such a short track (free from turbulence) could lead to an error from eight to sixty percent, depending on the scatter angle of the track, in the determination of the energy of the neutron associated with it. Accordingly, only tracks with dip angles less than fifty degrees were measured and the remaining tracks were accounted for by applying the weighting factor $f(\theta, \alpha_o = 50^o)$, based on the assumption of azimuthal symmetry, to each track measured.

d. Scatter Angle Limitation. Consider the situation in which a proton is scattered through a large enough angle θ so that its energy T_p may be determined through a measurement on its range R in the gas. Table 3 shows how R varies with the energy T_n of the incident neutron for $\theta = 85^o$. In addition there are tabulated values for the neutron angle θ' in the center of mass system.

TABLE 3

T_n(Mev)	θ	θ'	T_p(Mev)	R(cm)
155	85°	9.4^o	1.09	1.4
200	85°	9.3^o	1.37	2.2
300	85°	9.0^o	1.96	4.0

Since it was felt that tracks with $R \leq 1.4$ cm. might be overlooked, tracks for which $\theta = 85^o$ were rejected in the results of this paper, even though a few were measured for deflection angles up to 86° to make sure that no tracks were missed.

5. RESULTS AND CONCLUSIONS

For the neutron spectrum 1435 tracks were selected from the angular group ($0^o \leqslant \theta' \leqslant 85^o$ and $0^o \leqslant \alpha \leqslant 25^o$) for which the energy measurements are best. The results are shown in Table 4. The omission of tracks with dip angles greater than 25° is accounted for by multiplying each track measured by the correction factor $f(\theta, \alpha_o = 25^o)$ (See equation (6).). Also, a correction is made on the data for the variation[3] of the cross section with energy. A constant cross section of 37.08 millibarns corresponding to the value for 290 Mev was used for those neutrons which fall into energies above 350 Mev, since they presumably appear there through errors in measurements. Figure 10 gives a histogram of the data along with statistical error for each 20 Mev group of neutrons. In Fig. 11 the errors in measurement have been unfolded (See Appendix A 3.) from the histogram (2) to give the true spectrum (3). The peak of the spectrum from the 1-3/4 in. thick lithium-deuteride target occurs at 307 Mev. Curve (1), which is normalized to contain the same number of neutrons as curve (3), represents the neutron spectrum of Ball[11] and Hess from a 1/2 in. thick lithium-deuteride target. The agreement is excellent since one expects a slightly greater energy loss for the protons in the thicker target and, subsequently, a greater broadening of the neutron spectrum than for the case of the thinner target.

The angular distribution data, consisting of 2057 tracks which lie in a restricted angle and energy range ($T_n \geq 200$ Mev, $0^o \leqslant \alpha \leqslant 40^o$, and $10^o \leqslant \theta' \leqslant 180^o$), is tabulated in Table 5, in ten degree intervals, for the neutrons in the center of mass system. Each track is weighted by the factor $f(\theta, \alpha_o = 40^o)$ to take into account the tracks ($\alpha > 40^o$) which are not included in the distribution. The average cross section $\sigma(\theta_1', \theta_2')$ in mb/steradian for any angular interval $\theta_1' \leqslant \theta' \leqslant \theta_2'$ is determined from the fraction $\Delta N(\theta_1', \theta_2')/N$ of the total number of tracks in the interval, from the solid angle factor $\Delta\omega(\theta_1', \theta_2') = 2\pi \left| \cos\theta_1' - \cos\theta_2' \right|$ for the

TABLE 4

Distribution in Energy of the Incident Neutrons

($0^o \leqslant \theta \leqslant 85^o$, $0^o \leqslant \alpha \leqslant 25^o$)

Mev	Number of Tracks	Weighted Number	σ(mb)	$\frac{N\sigma}{37.08}$
160-180	55	91.5	46.55	72.9
180-200	72	125.6	43.71	106.6
200-220	92	166.1	41.63	148.0
220-240	106	166.9	40.07	154.4
240-260	169	266.3	38.85	254.0
260-280	200	352.0	37.87	344.7
280-300	263	424.4	37.08	424.4
300-320	237	379.5	36.42	386.3
320-340	147	259.5	35.86	268.3
340-360	69	138.2		138.2
360-380	19	39.0		39.0
380-400	6	16.6		16.6

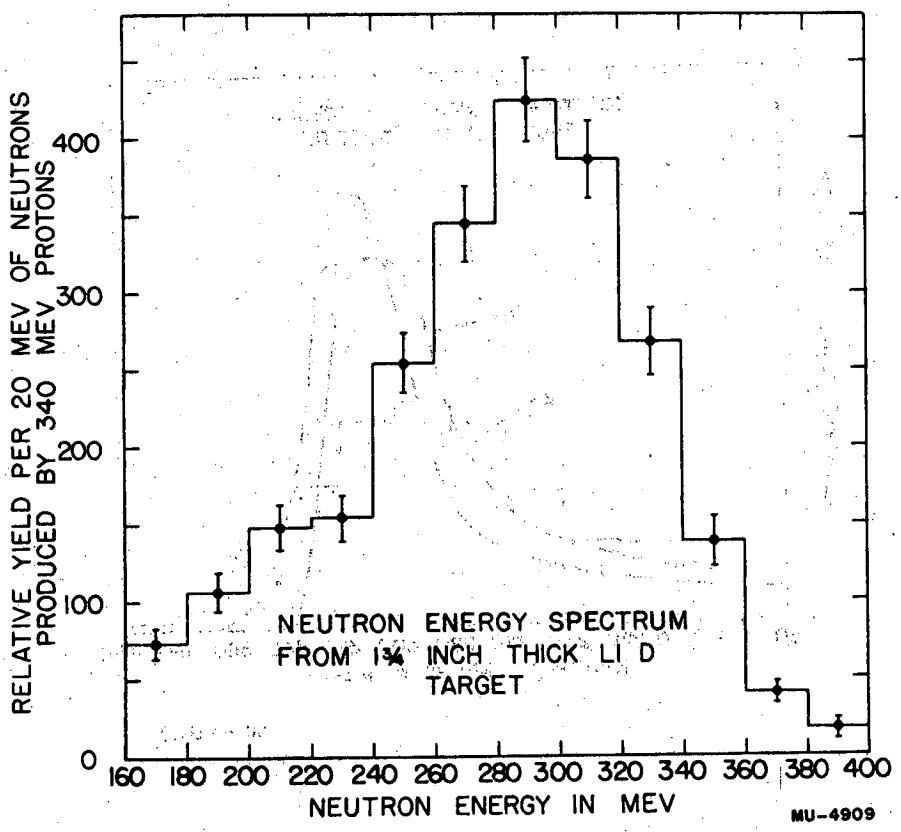

Fig. 10 The energy spectrum of neutrons produced in a 1-3/4 in. thick Li D target by 340 Mev protons before applying corrections for the errors in measurement.

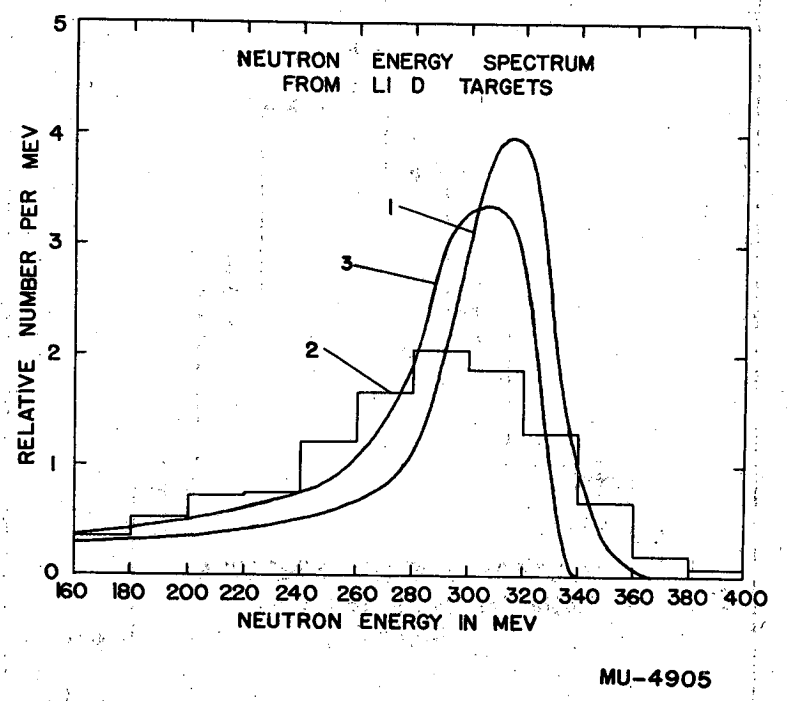

Fig. 11 The neutron energy spectra from two Li D targets of different thickness. Curve (1) shows the results of Ball and Hess for a 1/2 in. thick Li D target. Errors of measurement have been unfolded from the cloud chamber histogram (2) to yield the true spectrum (3) for the 1-3/4 in. thick Li D target.

TABLE 5

Angular Distribution of Neutrons in Center of Mass System

($0^o \leqslant a \leqslant 40^o$, $T_n \geqslant 200$ Mev)

Angle	Number of Tracks First Run	Number for Both Runs	Weighted Number	mb per Steradian
10-20	26	37	82.2	3.83 ± 0.63
20-30	42	56	121.9	3.48 ± 0.47
30-40	50	86	181.0	3.81 ± 0.41
40-50	70	102	205.2	3.50 ± 0.35
50-60	66	107	200.7	2.96 ± 0.29
60-70	70	98	173.5	2.31 ± 0.23
70-80	63	102	161.8	2.02 ± 0.20
80-90	78	112	155.6	1.89 ± 0.18
90-100	75	116	125.0	1.51 ± 0.14
100-110	104	166	166.0	2.07 ± 0.16
110-120	114	163	163.0	2.17 ± 0.17
120-130	90	170	170.0	2.51 ± 0.19
130-140	114	179	179.0	3.06 ± 0.23
140-150	118	193	193.0	4.06 ± 0.29
150-160	98	165	165.0	4.71 ± 0.37
160-170	81	139	139.0	6.48 ± 0.55
170-180	36	66	66.0	9.14 ± 1.12

interval, and from the total cross section σ_T mb, according to the formula $\sigma(\theta_1', \theta_2') \Delta\omega(\theta_1', \theta_2') = \sigma_T \Delta N(\theta_1', \theta_2')/N$. In order to compare the results of this experiment with those of Kelly, et al.,[6] σ_T was chosen to be 35 mb. Figure 12 shows a histogram of the angular distribution data along with the statistical errors for each ten degree group of neutrons. In Fig. 13, the experimental points of Kelly, et al.,[6] who employ a counter technique, are compared with the cloud chamber data. The agreement in the two sets of data is good. The special point (solid circle) at 175° is calculated from the counter data by integrating under a smooth curve drawn through it over the interval $170° \leqslant \theta' \leqslant 180°$ and then by dividing the result obtained by the solid angle for the interval. Figure 14 shows the comparison with theory. The disagreement between the experimental data (1) and the curves[10] representing the theories of Christian and Hart[7] (2), Jastrow[9] (3) and Christian and Noyes[8] (4) is particularly striking for small neutron scatter angles.

Table 6 lists some angular distribution data ($T_n \geqslant 200$ Mev, $0° \leqslant \alpha \leqslant 50°$, $10° \leqslant \theta' \leqslant 180°$) which is considered to be less reliable (see Section 5 on experimental checks.) than the data which has been presented in Table 5. The data, consisting of 2189 tracks, has been corrected for the tracks not measured ($\alpha \geqslant 50°$), by applying the weighting factor $f(\theta, \alpha_o = 50°)$ to each track. The process of normalizing the data to 35 mb has been discussed previously.

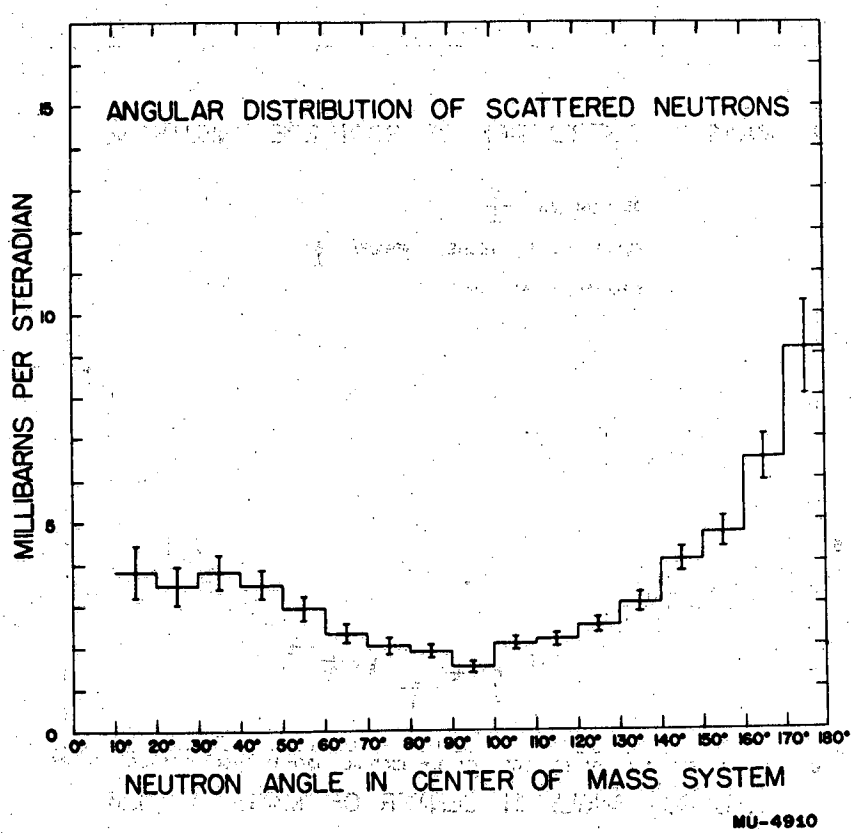

Fig. 12 The histogram shows the angular distribution of neutrons in the center of mass system for a restricted angle and energy range ($T_n \geqslant 200$ Mev, $0^\circ \leqslant \alpha \leqslant 40^\circ$, $10^\circ \leqslant \theta \leqslant 180^\circ$).

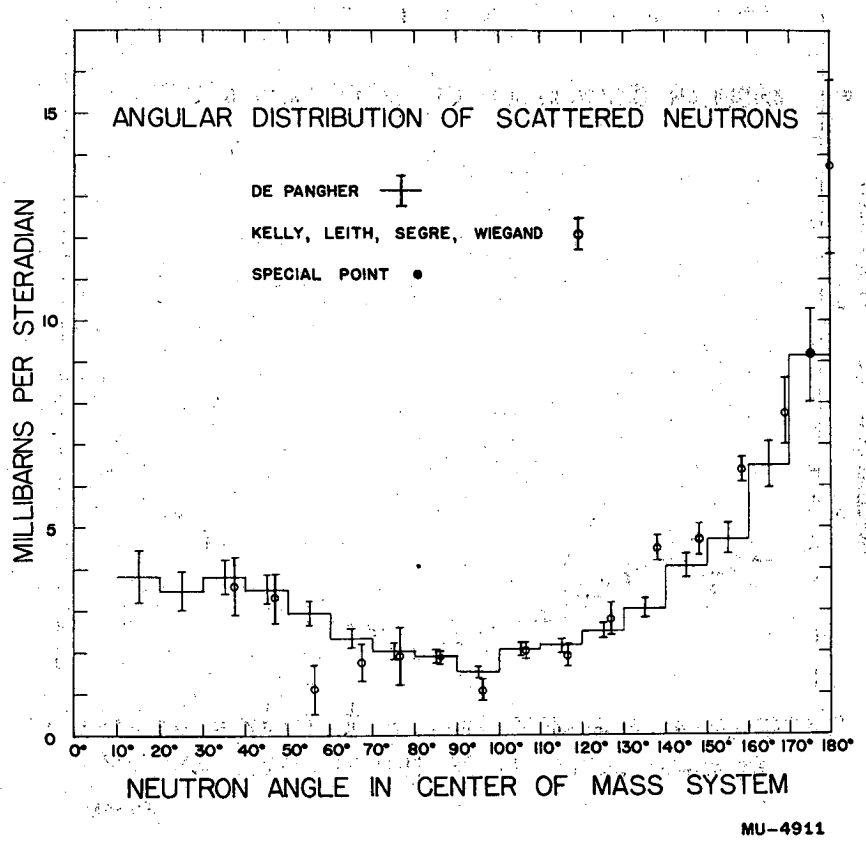

Fig. 13 Two sets of data are displayed here, the cloud chamber work (histogram) and the experimental points of Kelly et al.[6] on the angular distribution of neutrons in the center of mass system. The meaning of the special point is given in the text.

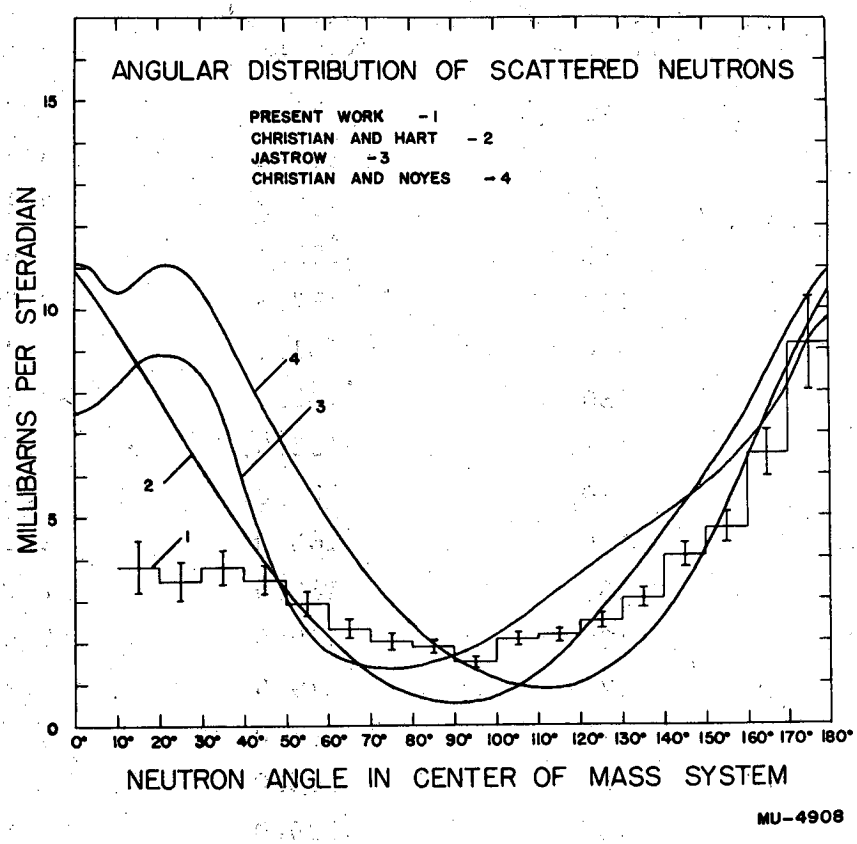

Fig. 14 The experimental data is compared here with the results of calculations[10] from three theories.[7,8,9] The disagreement between theory and experiment is strikingly evident for small neutron scatter angles.

TABLE 6

Angular Distribution of Neutrons in Center of Mass System

($0^{o} \leqslant \alpha \leqslant 50^{o}$, $T_n \geqslant 200$ Mev)

Angle	Number of Tracks	Weighted Number	mb per Steradian
10-20	40	69.1	3.41 ± 0.54
20-30	69	119.1	3.60 ± 0.43
30-40	97	161.2	3.59 ± 0.36
40-50	123	192.1	3.47 ± 0.31
50-60	123	177.3	2.76 ± 0.25
60-70	114	151.0	2.13 ± 0.20
70-80	130	140.1	1.85 ± 0.16
80-90	133	133.0	1.70 ± 0.15
90-100	119	120.0	1.54 ± 0.14
100-110	166	166.0	2.19 ± 0.17
110-120	163	163.0	2.30 ± 0.18
120-130	170	170.0	2.65 ± 0.20
130-140	179	179.0	3.23 ± 0.24
140-150	193	193.0	4.29 ± 0.31
150-160	165	165.0	4.98 ± 0.39
160-170	139	139.0	6.85 ± 0.58
170-180	66	66.0	9.67 ± 1.19

6. MESON EVENTS

A search was made for the following types of reactions in which mesons are produced: (1) $n + p \rightarrow \pi^- + p + p$, (2) $n + p \rightarrow \pi^+ + n + n$ and (3) $n + p \rightarrow \pi^o + d$. No events of type (1) were observed. The one event of type (2), in which the π^+ meson starts in the collimated region of the chamber and makes a complete revolution before it passes out of the chamber, is shown in Fig. 15. Six deuterons, identifiable from ionization and curvature, were observed starting in the collimated region of the chamber. One of these deuterons (95 ± 29 Mev), making a wide angle (51.5°) with the direction of the neutron beam, arose from an elastic scatter of a neutron by a deuteron existing as an impurity (one part in 5,000) in the gas of the cloud chamber. A second deuteron (116.6 ± 7.0 Mev) very likely demonstrates radiative capture ($n + p \rightarrow \gamma + d$) since its angle (9.5 ± 0.5°) exceeds the maximum angle of 7° required by the energetics of the type (3) reaction. The four remaining deuterons (energies 117-226 Mev, angles 2.0°-3.4°) satisfy the energetics of either the type (3) reaction or the energetics of the radiative capture process. (It is quite improbable that any of the deuterons which lie in a cone of aperture 10° around the direction of the neutron beam arise from gas impurities since the solid angle subtended by the cone is only 1.5 percent of the total solid angle for elastic scattering.) An estimate of the radiative capture cross section for 300 Mev neutrons on protons yields 1.0×10^{-29} cm^2. (This result is obtained by applying the method of detailed balancing[14] to the data by Gilbert[15] on the photodisintegration of the deuteron at high energies.) The cross section for the four deuterons can be estimated from the known cross section for elastic n-p scattering and from the number of protons which were measured to give neutron energies, say, greater than 270 Mev. The result is $(8 \pm 4) \times 10^{-29}$ cm^2. Since this cross section is at least four times as large as the estimated radiative capture cross section, we conclude that some of these deuterons, if not all of them, were accompanied by neutral mesons. Figs. 16 and 17 show photographs of deuterons starting in the gas of the chamber.

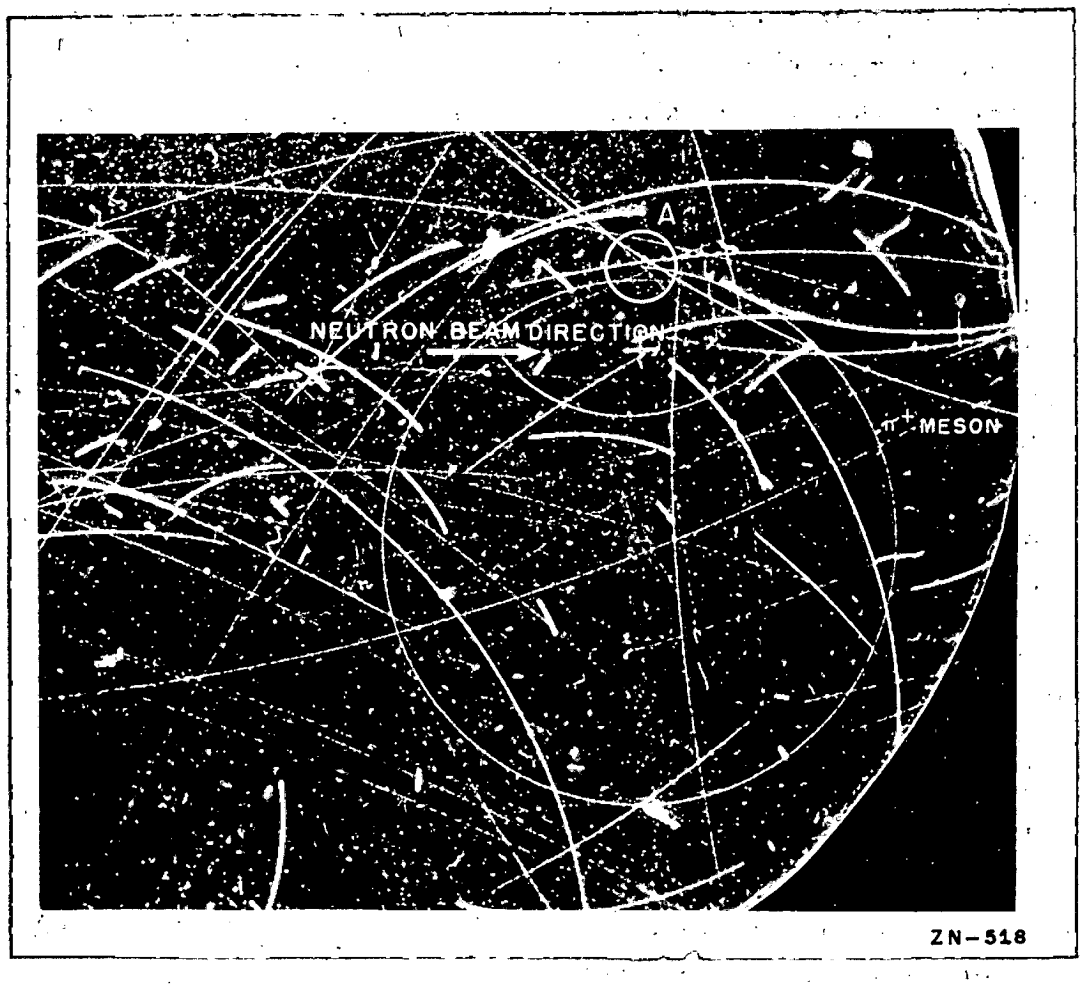

Fig. 15 Cloud chamber picture. An example of the reaction $n + p = \pi^+ + n + n$. The π^+ meson, 4 Mev, starts at the center of the circle A and makes one complete revolution in the chamber before leaving it.

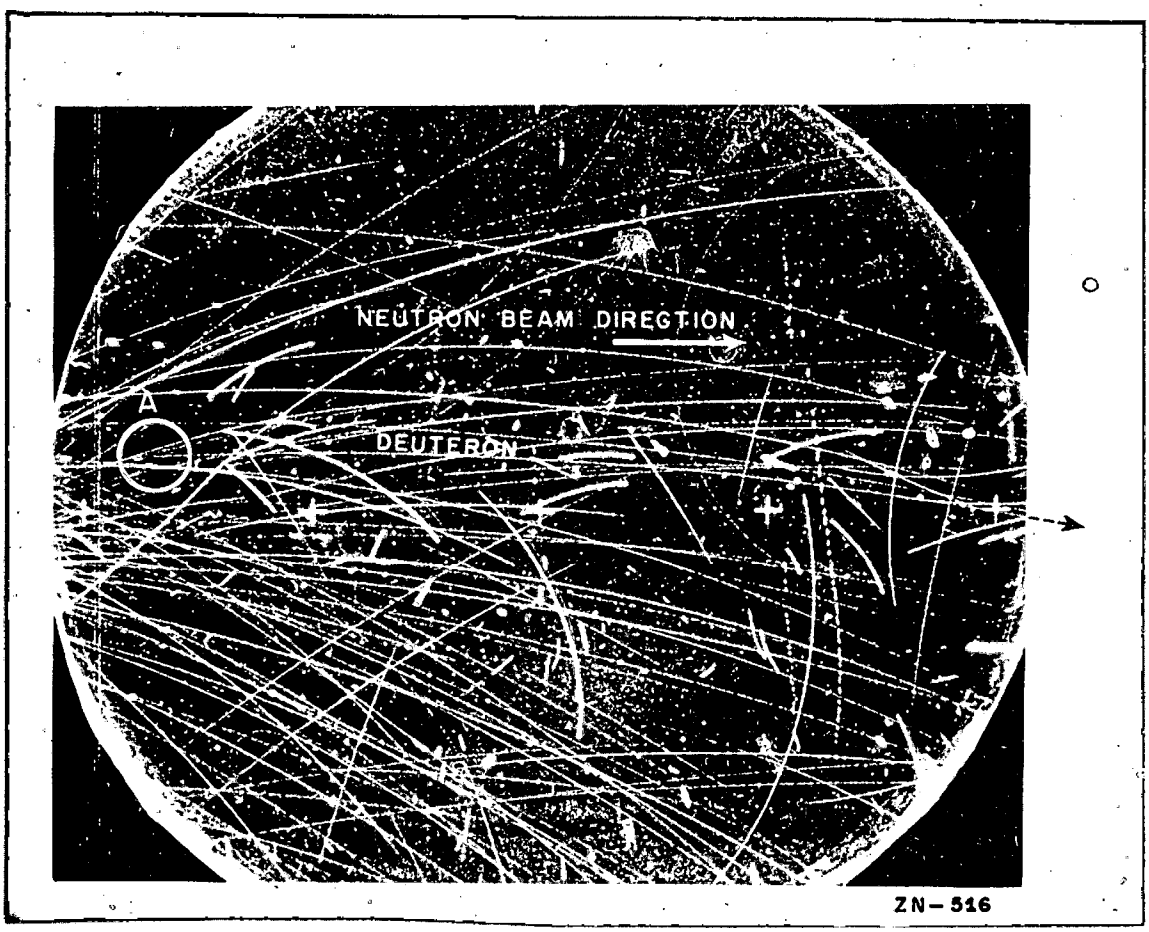

Fig. 16 Cloud chamber picture. The deuteron which starts at the center of the circle A probably is a product of the reaction $n + p = \pi^o + d$.

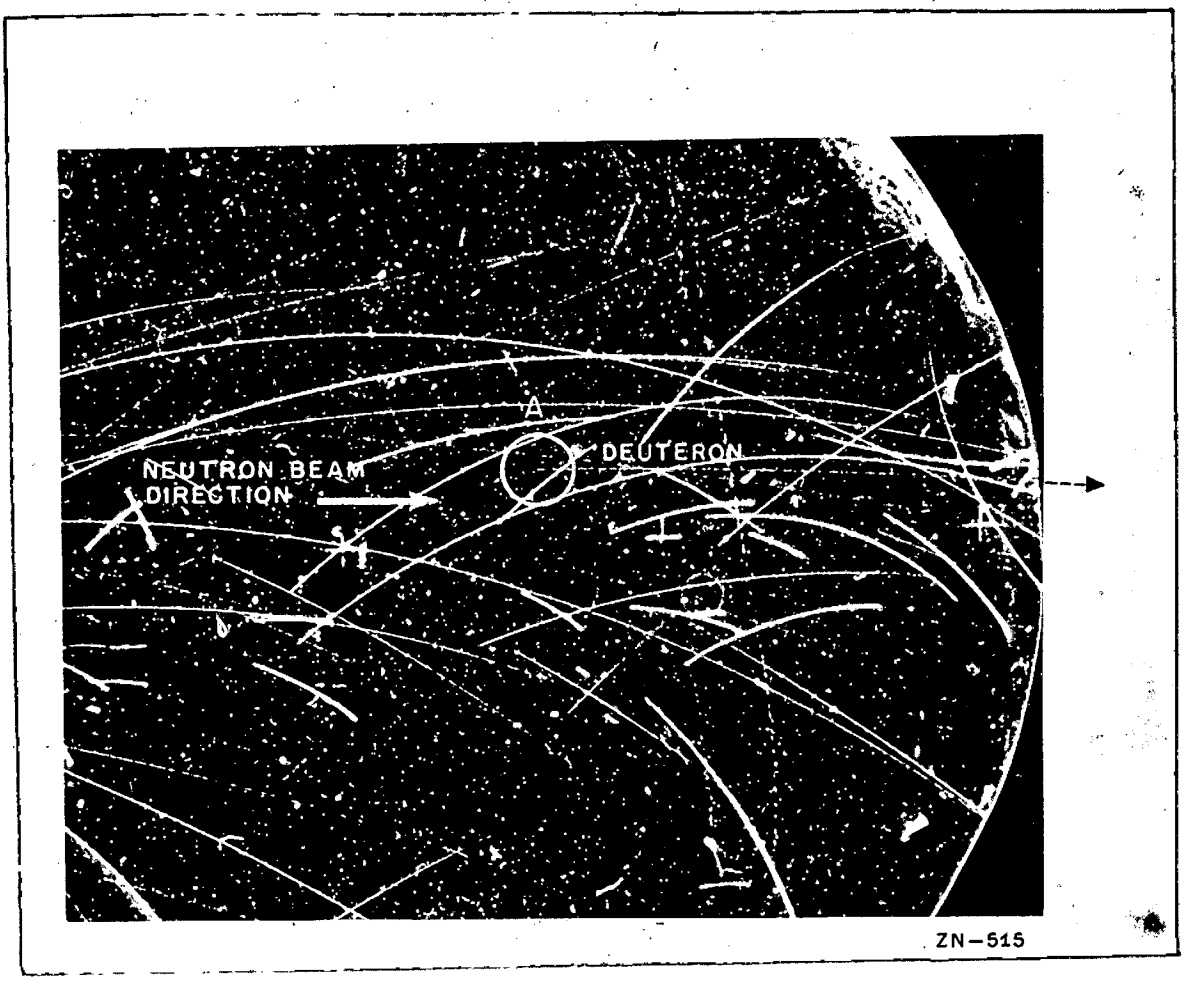

Fig. 17 Cloud chamber picture. The deuteron which starts at the center of the circle A probably is a product of the reaction $n + p = \pi^o + d$.

7. EXPERIMENTAL CHECKS AND DISCUSSION OF ERRORS

Generally, the highest energy proton tracks are clearly visible everywhere in the illuminated region of the chamber. However, some sections of film, taken at times when adjustments were being made to determine the best operating conditions for the chamber, exhibit high energy tracks which are faint near the cover glass. Accordingly, a rule was adopted to reject pictures unless they contained high energy tracks clearly visible up to a distance 1/4 in. from the cover glass.

As mentioned previously, there are limits imposed on the curvature and dip angle of a track, and on the region in which it starts before it is accepted. A portion of the data, already measured by the writer, was selected and measured independently by a second observer who followed the same limits. He found that the writer had missed two tracks in a hundred measured. The two sets of measurements were reproducibile to $\pm 1.5^{\circ}$ in the dip angle and to $\pm 0.5^{\circ}$ in the beam angle. In addition, calculations on the sagitta of each track showed that the sagittae were reproducible to ± 0.005 cm. A stereoscopic viewer, recently developed, with magnification and illumination characteristics superior to those of the reprojection apparatus, provided the author with a rapid and a psychologically different method of scanning the film. Another section of film was scanned with the viewer; misses were observed and then were measured on the reprojection apparatus. Five acceptable tracks in 250 were found which previously had been overlooked. Of the seven tracks in 350 which had been overlooked, four had dip angles in the range $40^{\circ} \leqslant \alpha \leqslant 50^{\circ}$. On the basis of this sampling procedure, as applied to the 2,189 tracks which are included in the angular distribution ($\alpha \leqslant 50^{\circ}$, $T_n \geqslant 200$ Mev), it is estimated that a total of 44 ± 17 tracks have been overlooked with 25 ± 9 tracks lying in the interval $40^{\circ} \leqslant \theta \leqslant 50^{\circ}$. In particular, for the range of angles $40^{\circ} \leqslant \theta \leqslant 50^{\circ}$, $45^{\circ} \leqslant \phi \leqslant 135^{\circ}$, and $225^{\circ} \leqslant \phi \leqslant 315^{\circ}$ two tracks were found missing in 350; therefore we estimate a total number 12 ± 8 to be missing.

The possibility of confusing recoil protons with two-pronged oxygen stars (where the recoil nucleus is a tiny blob at the origin of the star) has been investigated. Ford[18] (in connection with his cloud chamber work on the disintegration of oxygen by 300 Mev neutrons) read a portion of the writer's film. He estimated that approximately 120 oxygen stars were present in the data. Furthermore he states, from experience with his own data, that twelve of these stars should have two prongs. This result is not inconsistent with the result obtained by the writer, so it is concluded that no confusion arises from the presence of oxygen in the chamber.

Although the accuracy of the reprojection apparatus has been checked previously an additional check on it was made in the following way. Fig. 18 shows a double-scattering event in the gas of the cloud chamber. A neutron collides with a proton and the proton moves on to collide with another proton. Several pictures containing events of this type have been found. One of these (not the one shown in Fig. 18) was measured to determine the angles of the three protons. The calculation, based on these measurements, of the angle between the scattered protons leads to a value which agrees, within the previously stated errors of measurements, with a value predicted from the study of the relativistic kinematics of the situation.

One picture in ten was taken without the magnetic field. An investigation of the radius of curvature ρ_t arising from turbulence in the tracks lying near the horizontal plane was made by measuring 92 tracks contained in these pictures on a precision travelling microscope. The curvatures were measured by plotting the track on a scale enlarged in the direction of the sagitta so that it could be measured more accurately. The distribution in curvatures $C_t = 1/\rho_t$ is Gaussian with the standard deviation $C_t = (33m)^{-1}$. It is assumed that this result can be applied to an error analysis of tracks whose lengths are greater than 8 cm. and whose dip angles do not exceed 25°. For shorter tracks we assume, on the basis of the most turbulent tracks measured in the above group, a

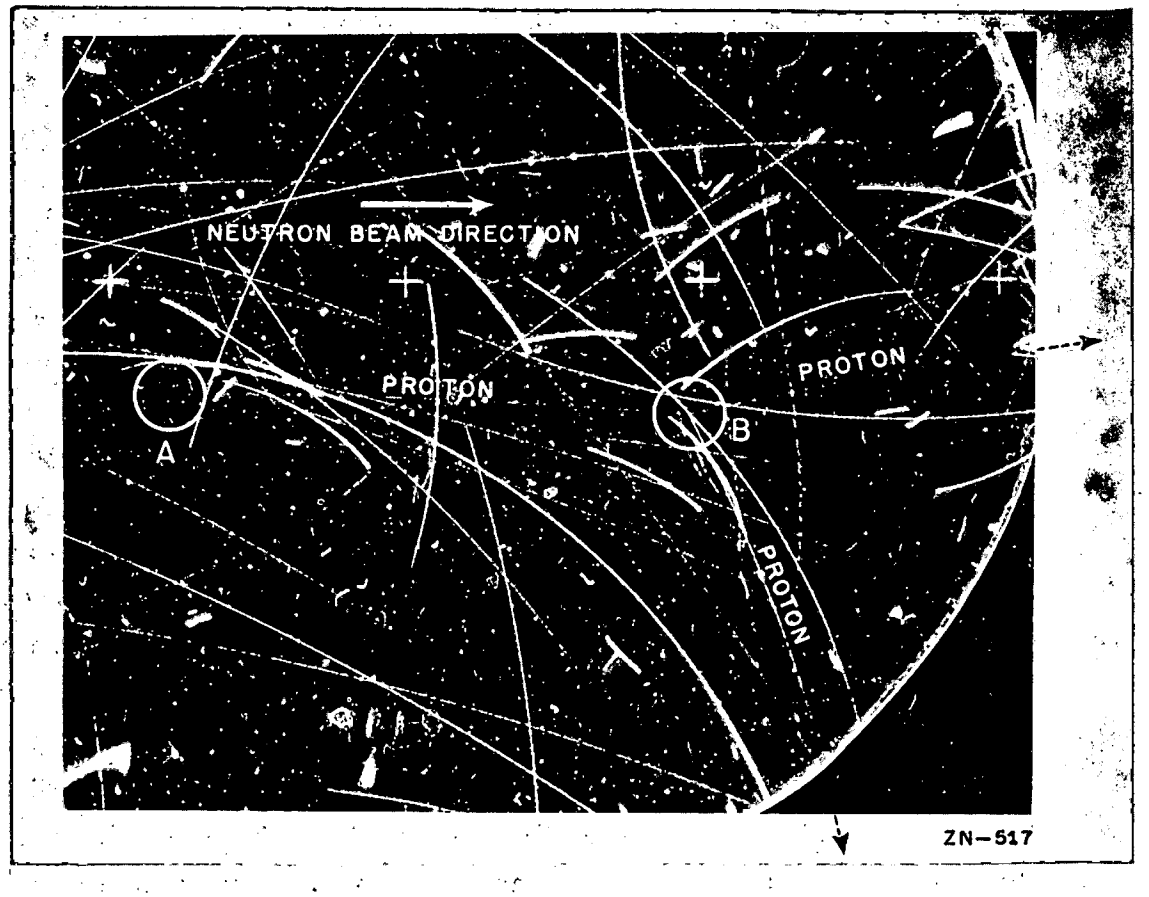

Fig. 18 Cloud chamber picture. A neutron collides with a proton at the center of circle A. The proton moves on and collides with a second proton at the center of the circle B. This double-scatter event can be used to check the accuracy of the reprojection apparatus.

standard deviation $C_t = (23\ m)^{-1}$. Steeper dipping tracks in the ranges of dip angle $30^o \leqslant \alpha \leqslant 40^o$ and $40^o \leqslant \alpha \leqslant 50^o$ were found to possess turbulence curvatures up to $C_t = \pm (4\ m)^{-1}$ and $C_t = (1.2\ m)^{-1}$ from measurements on the no-field pictures in the reprojection apparatus. (Lucite templates were used to measure these curvatures.) The shape of the distribution function assumed is given in Fig. 19. (See also discussion in Appendix A 5.)

The distribution of tracks in azimuthal angle for $\alpha \leqslant 50^o$ is shown in Fig. 20. Tracks which fall into the excluded region ($\alpha \geqslant 50^o$) are not measured but may be accounted for by applying the correction factor $f(\theta, \alpha_o = 50^o)$ to the tracks which are measured. The number of tracks for any square or partial square is given in the square. The numbers within any vertical column and contained in whole squares should agree within the statistical errors of measurement if the azimuthal distribution is considered to be uniform. An analysis of these numbers shows that they are sufficiently uniform to substantiate the assumption of azimuthal symmetry except for those numbers which lie in squares near the excluded region. In particular, let us look at the vertical column of numbers which represents tracks which lie in the range of angles $40^o \leqslant \theta \leqslant 50^o$. A first set of squares is defined by the range of azimuthal angles $45^o \leqslant \phi \leqslant 135^o$ and $225^o \leqslant \phi \leqslant 315^o$. They contain 27 + 30 + 18 + 19 = 94 tracks. The energy measurements on this group of tracks are relatively poor because of the presence of the comparatively large turbulence in this region of the chamber. Consider the remaining squares which contain 26 + 42 + 36 + 48 = 152 tracks. The energy measurements on this second group of tracks are considered to be quite accurate as they are inclined at relatively small angles to the horizontal plane where very little turbulence is present. We estimate that 152-94 tracks are missing from the first group. Now we want to account for this deficiency. Twelve of these tracks could have been overlooked (See second paragraph of this section.). Also, an estimated 0.36 x 152 = 55 (See Appendix A 5.) tracks have been omitted through errors in measurement of the neutron energies. The deficiency estimate 55 + 12 = 67 agrees reasonably well with the observed deficiency 58 so we conclude that the estimate of the errors is good.

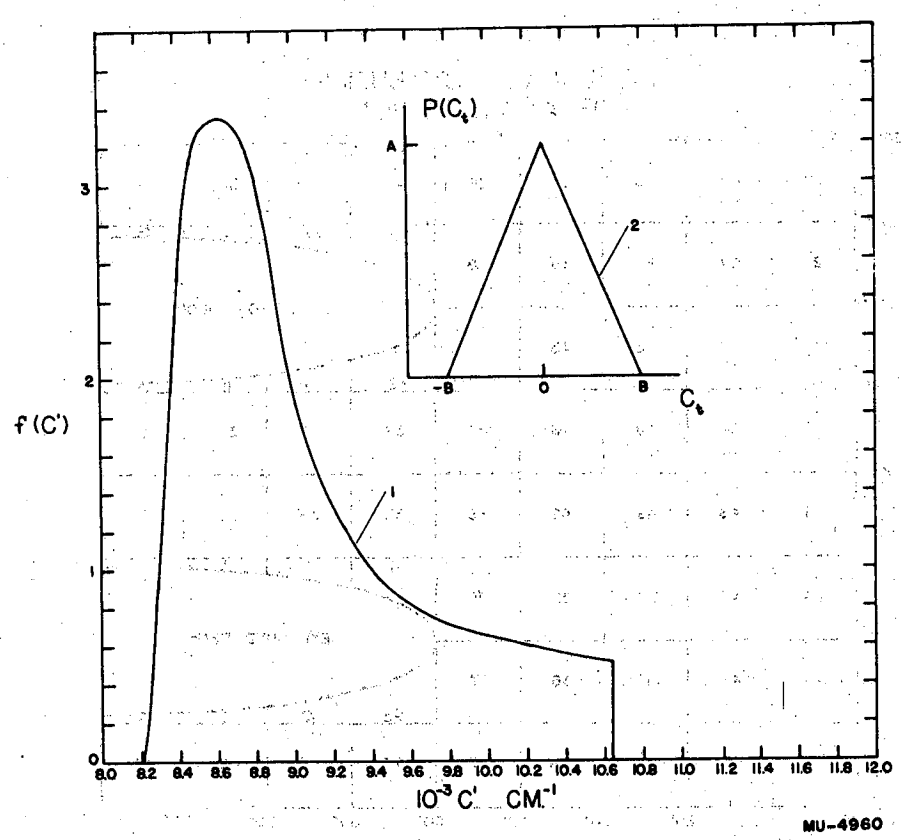

Fig. 19 Curvature spectrum and turbulence plot for the representative tracks described in Appendix A 5.

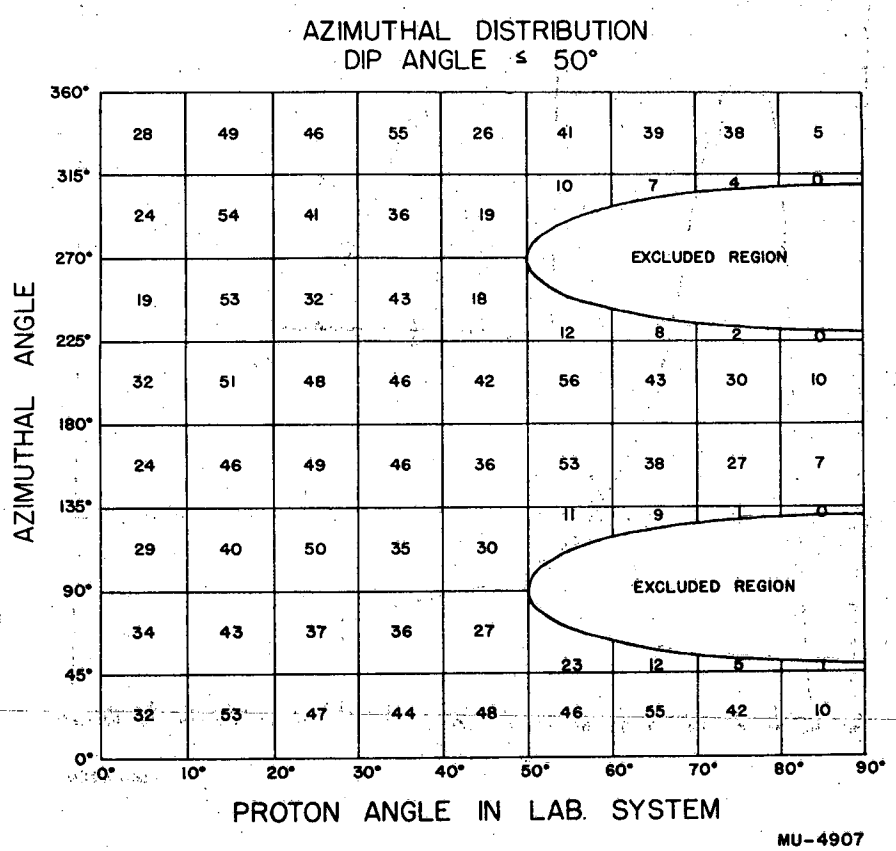

Fig. 20 Azimuthal distribution for $\alpha \leq 50^{\circ}$. The excluded region is enclosed by the curve $\sin\theta \sin\phi = \sin 50^{\circ}$.

Let us consider a third group of squares ($30^o \leqslant \theta \leqslant 40^o$, $45^o \leqslant \phi \leqslant 135^o$, $225^o \leqslant \phi \leqslant 315^o$). The analysis of Appendix A 5 shows that ten percent of these tracks are expected to be missing through errors in measurement arising from turbulence. However, this ten percent loss shows up as only a five percent loss in the total number of tracks for the eight squares.

Since the number of tracks with dip angles greater than 40° appear to be in doubt, they are excluded from the data. Figure 21 shows the azimuthal distribution for $\alpha \leqslant 40^o$. Although it still contains portions of the track-deficient squares the total number of tracks in the vertical column is only diminished now by about twelve percent. It is to be compared with the adjacent group which displays a deficiency of five percent.

Figures 22 shows an aximuthal diagram in whose squares are entered the quantities p(300), q, and $(p^2 + q^2)^{1/2}$, which have been obtained by applying an averaging process to each square (See Appendix A 2.). They represent, respectively, the energy-dependent error, the angle-dependent error and the total error in the measurement of the energy of a 300 Mev neutron (See Appendix A 4.).

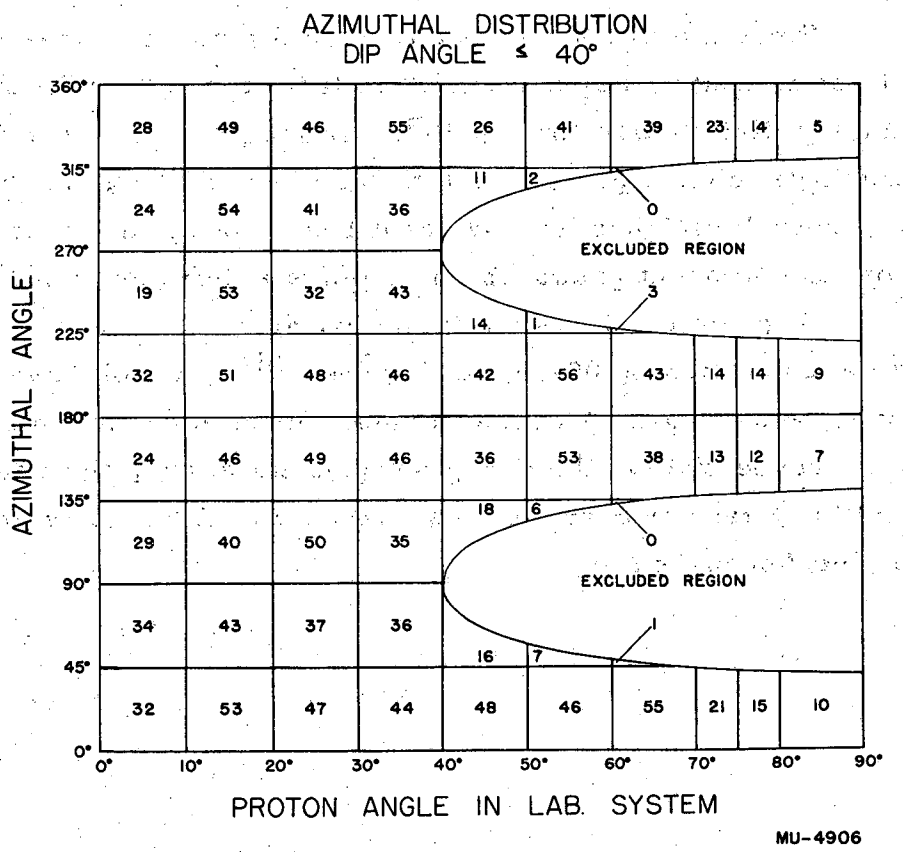

Fig. 21 Azimuthal distribution for $\alpha \leqslant 40^{\circ}$. The excluded region is enclosed by the curve $\sin\theta \sin\phi = \sin 40^{\circ}$.

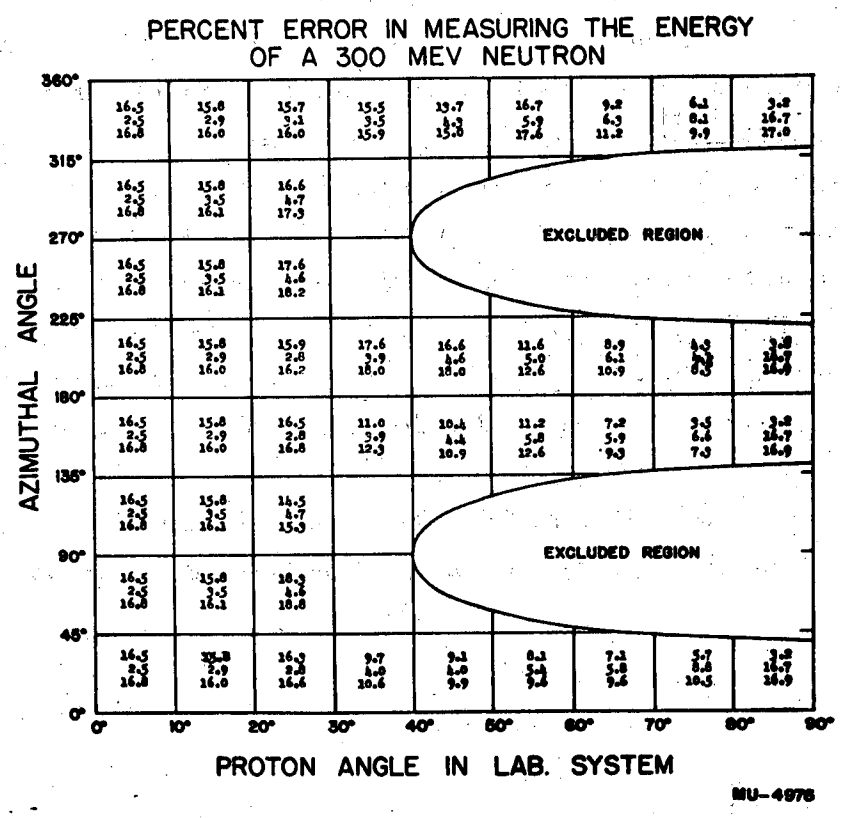

Fig. 22 Errors in the measurements of a monoenergetic neutron beam of energy E' = 300 Mev. The percentage errors p(300); q and $(p^2 + q^2)^{1/2}$ which are written in any square are based on the Gaussian errors in measurement on the tracks contained in the square. Some squares are vacant; the non-Gaussian errors for them are calculated in Appendix A-5.

REFERENCES

1. J. E. Brolley, Jr., J. H. Coon, and J. L. Fowler, Phys. Rev. 82, 190 (1951).

2. J. Hadley, E. Kelly, C. Leith, E. Segrè, C. Wiegand, and H. York, Phys. Rev. 75, 351 (1948).

3. K. Brueckner, W. Hartsough, E. Hayward, and W. M. Powell, Phys. Rev. 75, 555 (1948).

4. T. C. Randle, A. E. Taylor, and E. Wood, Proc. Roy. Soc. (London) 213, 392 (1952).

5. G. R. Mott, G. L. Guernsey, and B. K. Nelson, Phys. Rev. 88, 15 (1952).

6. E. Kelly, C. Leith, E. Segrè, and C. Wiegand, Phys. Rev. 79, 96 (1950).

7. R. S. Christian and E. W. Hart, Phys. Rev. 77, 441 (1950).

8. R. S. Christian and H. P. Noyes, Phys. Rev. 79, 85 (1950).

9. R. Jastrow, Phys. Rev. 79, 389 (1950).

10. O. Chamberlain, E. Segrè, and C. Wiegand, Phys. Rev. 83, 923 (1951).

11. W. P. Ball, UCRL-1938.

12. W. M. Powell, Rev. Scient. Inst., 20, 403 (1949).

13. W. A. Aron, B. G. Hoffman, F. C. Williams, UCRL-121.

14. H. A. Bethe, Elementary Nuclear Theory, p. 61, John Wiley and Sons, Inc., 1947.

15. W. Gilbert, UCRL-1590.

16. A. S. Levens, Nomography, John Wiley and Sons, Inc., 1948.

17. R. D. Douglass, D. P. Adams, Elements of Nomography, McGraw-Hill Book Company, Inc., 1947.

18. F. Ford, private communication.

APPENDIX A

1. Derivation of the Formula for the Error in the Energy of a Neutron

An approximate expression[3] for the fractional standard error in the energy of a neutron may be obtained by differentiating the non-relativistic formula for the neutron energy

$$T_n = \frac{e^2}{2\,Mc^2}\left(\frac{B\,\rho_s}{\cos\beta}\right)^2$$

to yield

$$\frac{\delta T_n}{T_n} = 2\left[\left(\frac{\delta B}{B}\right)^2 + \left(\frac{\delta\rho_s}{\rho_s}\right)_N^2 + (\tan\beta\,\delta\beta)^2\right]^{1/2} .$$

(The symbols have already been defined in the text.) The net fractional error $(\delta\rho_s/\rho_s)_N$ in the curvature of the proton track associated with the neutron depends on (1) the dip angle error $\delta\alpha$, on (2) the uncertainty $(\delta\rho_s/\rho_s)_M$ which appears in matching one of the set of arcs on the Lucite template to the track and on (3) the error ρ_s/ρ_t which arises from a turbulence radius of curvature ρ_t. Since the slant radius ρ_s is related[3] to ρ_H, the radius of the track if it is measured in a horizontal plane, by the expression $\rho_H = \rho_s \cos^2\alpha$ one can deduce the error expression

$$\left(\frac{\delta\rho_s}{\rho_s}\right)_N = \left[(2\tan\alpha\,\delta\alpha)^2 + \left(\frac{\delta\rho_s}{\rho_s}\right)_M^2 + (\rho_s/\rho_t)^2\right]^{1/2} .$$

If we assume that the problem of measuring ρ_s for a track is a matter of measuring a sagitta t for a chord of length L, then for a sagitta error $\delta t = \pm\,0.005$ cm. the matching error is

$$\left(\frac{\delta\rho_s}{\rho_s}\right)_M = \frac{8\,\rho_s\delta t}{L^2} = \frac{0.04\,\rho_s}{L^2} .$$

By employing the non-relativistic forms of equations (7) and (8) in the text

$$\rho_s = \rho \cos \beta$$

and

$$\rho = \frac{10^4}{3B} (1876\ T_n)^{1/2}$$

we can put the matching error in the form

$$\left(\frac{\rho_s}{\rho_s}\right)_M = \frac{0.04\ \rho \cos \beta}{L^2}.$$

The various errors are collected together to give the total fractional error

$$\frac{\delta T_n}{T_n} = 2\left[\left(\frac{\delta B}{B}\right)^2 + (2 \tan \alpha \delta \alpha)^2 + (\tan \beta \delta \beta)^2 + \left(\frac{0.04\ \rho \cos \beta}{L^2}\right)^2 + \left(\frac{\rho \cos \beta}{\rho_t}\right)^2\right]^{1/2}$$

in the neutron energy. We now define the functions

$$F(\beta,\ L,\ \rho_t) = 2 \cos \beta \left[\left(\frac{0.04}{L^2}\right)^2 + \left(\frac{1}{\rho_t}\right)^2\right]^{1/2}$$

and

$$G(B,\ \alpha,\ \beta) = 2\left[\left(\frac{\delta B}{B}\right)^2 + (2 \tan \alpha \delta \alpha)^2 + (\tan \beta \delta \beta)^2\right]^{1/2}$$

and calculate the curvature ρ for a magnetic field strength $B = 21,700$ gauss. The result is

$$\rho = 66.54\ (T_n)^{1/2}$$

Finally, the formula for the fractional error in the measurement of the neutron energy is

$$\frac{\delta T_n}{T_n} = (\rho^2 F^2 + G^2)^{1/2}$$

where ρ is the only variable which depends on the neutron energy.

2. Energy Resolution of the Cloud Chamber

The analysis of errors in this section applies to Gaussian errors only and makes use of the formula derived in Appendix A 1 for the fractional standard error in the measurement of the energy of a neutron.

Consider a beam of monoenergetic neutrons of energy E' which enters the cloud chamber and produces recoil protons in the gas. If the neutron associated with the ith track has the fractional standard error in energy σ_i and the ith track has the weighting factor f_i (See Appendix B.), then the spectrum which results from the measurements on $\sum_i f_i = N$ weighted tracks is characterized by a standard error σ. The following expression

$$\sigma = \left(\frac{\sum_i f_i \sigma_i^2}{N} \right)^{1/2}$$

holds true for Gaussian errors.

Since the final result of Appendix A 1 gives

$$\sigma_i = (\rho^2 F_i^2 + G_i^2)^{1/2}$$

we can calculate σ from

$$N \sigma^2 = \sum_i f_i (\rho^2 F_i^2 + G_i^2) = \rho^2 (\sum_i f_i F_i^2) + (\sum_i f_i G_i^2).$$

Let us define quantities a and by by the equations

$$a = (66.54)^2 (\sum_i f_i F_i^2)/N$$

$$b = (\sum_i f_i^2 G_i^2)/N$$

They are constants of the cloud chamber for the experiment being performed. Since $\rho(E') = 66.54 (E')^{1/2}$ we may express σ in the form

$$\sigma(E') = (aE' + b)^{1/2}.$$

The quantities a and b may be determined by calculating the errors in measurement for a large number of tracks and by assuming that the angular distribution of these tracks is essentially independent of the neutron energy E'.

3. Operation of Unfolding Errors of Measurement from the Experimental Neutron Spectrum

Let $K(E, E')$ be the experimental error function, normalized to unity, which removes a neutron from its correct position in an energy interval dE' about E' to the observed interval dE about E. If $f(E')$ is the true spectrum and $F(E)$ is the observed spectrum, then the number of neutrons which are observed in any interval $E_1 \leqslant E \leqslant E_2$ is given by

$$N(E_1, E_2) = \int_{E_1}^{E_2} F(E)\, dE = \int_{E_1}^{E_2} \int_{E_1'}^{E_2'} K(E, E')\, f(E')\, dE'\, dE$$

where the true spectrum extends over the range $E_1' \leqslant E' \leqslant E_2'$. Let us approximate the integral over E' by a sum over small but finite intervals $\delta E'$. If $\delta n(E') = f(E')\delta E'$ is the number of neutrons which lie in any finite interval $\delta E'$ of the true spectrum, we may write, approximately

$$N(E_1, E_2) = \sum_{E'} \delta n(E') \int_{E_1}^{E_2} K(E, E')\, dE$$

By choosing the interval $E_1 \leqslant E \leqslant E_2$ to be small we may replace $N(E_1, E_2)$ by $\delta N(E) = F(E)\, \delta E$ and arrive at an approximate expression for the measured spectrum:

$$F(E) = \sum_{E'} \frac{\delta n(E')}{\delta E} \int_{E - \frac{\delta E}{2}}^{E + \frac{\delta E}{2}} K(E, E')dE$$

The errors in measurements on the neutron spectrum are Gaussian so the error function has the form

$$K(E, E') = \frac{1}{(2\pi)^{1/2}\, \Delta}\, e^{-\frac{(E - E')^2}{2\Delta^2}}$$

The standard error Δ Mev is a function of E'; it is related to the fractional standard error σ(see Appendix A 2.) by the formula $\Delta(E') = E'\, \sigma(E')$. A

calculation (The method is outlined in Appendix A 2.) of the errors in measurement on 159 tracks of the type used for the neutron spectrum lead to the empirical formula

$$\Delta(E') = E' (0.00241\, E' + 0.223)^{1/2}$$

The expression for F(E) is now

$$F(E) = \sum_{E'} \frac{\delta n(E')}{\delta E} \int_{E - \frac{\delta E}{2}}^{E + \frac{\delta E}{2}} \frac{1}{(2\pi)^{1/2}\, \Delta} e^{-\frac{(E - E')^2}{2\Delta^2}} dE$$

If we make a change of variable $t = (E - E')/\Delta$ and set $t^+ = (E + 1/2\,\delta E - E')/\Delta$, $t^- = (E - 1/2\,\delta E - E')/\Delta$, and

$$I(t^+, t^-) = 1/(2\pi)^{1/2} \int_{t^-}^{t^+} e^{\frac{-t^2}{2}} dt$$

we get the expression

$$F(E) = \sum_{E'} \frac{\delta n(E')}{\delta E} I(t^+, t^-)$$

from which calculations can easily be made. A table of values for $I(t^+, t^-)$ was constructed in the following way: (1) energy intervals $\delta E' =$ 10 Mev and $\delta E = 20$ Mev were chosen; (2) t^+ and t^- were calculated from the values of E and E' at the midpoints of these intervals; (3) finally, tables of the probability integral were consulted to obtain $I(t^+, t^-)$. For the purpose of calculation f(E') was assumed to satisfy the conditions $f(E' < 160 \text{ Mev}) = f(E' > 340 \text{ Mev}) = 0$. The spectrum F(E) was calculated by assuming values for f(E') until a choice of f(E') lead to values of F(E) which agreed with the experimental spectrum. This choice of f(E') gives the unfolded spectrum (curve (3) in Fig. 11).

4. Loss of Neutrons through Lower Energy Boundary, Assuming Gaussian Errors of Measurement.

Consider the neutrons which are associated with tracks that fall into the azimuthal and scatter angle intervals $\phi_1 \leq \phi \leq \phi_2$ and $\theta_1 \leq \theta \leq \theta_2$. A certain number of these neutrons (true energies above 200 Mev) are thrown into energies below 200 Mev by errors in measurement and will appear missing from the azimuthal distribution (See Fig. 20.). This number can be estimated from the formula

$$N(E_1, E_2) = \sum_{E'} \delta n(E') \int_{E_1}^{E_2} K(E, E')\, dE$$

which was derived in Appendix A 3, if we set $E_1 = 0$ and $E_2 = 200$ Mev. The error function $K(E, E')$ is

$$K(E, E') = \frac{1}{(2\pi)^{1/2}\,\Delta}\, e^{-\frac{(E-E')^2}{2\Delta^2}}$$

where $\Delta(E') = E'(aE' + b)^{1/2}$. The constants a and b for tracks lying in the intervals $\phi_1 \leq \phi \leq \phi_2$ and $\theta_1 \leq \theta \leq \theta_2$ may be evaluated by employing the procedure of calculation outlined in Appendix A 2 to these tracks. Now let us introduce the percent errors $p(E') = 100\,(aE')^{1/2}$ and $q = 100\, b^{1/2}$, in the expression for Δ. The result is $\Delta(E') = 10^{-2}\, E' \left[p^2(E') + q^2\right]^{1/2}$. If we know a and b we can calculate $p(300) = 100(300a)^{1/2}$ and $q = 100b^{1/2}$. Finally, Δ may be written $\Delta(E') = 10^{-2}\, E' \left[p^2(300)E'/300 + q^2\right]^{1/2}$. Fig. 22 gives p(300), q, and $(p^2 + q^2)^{1/2}$ for groups of tracks in the angular distribution. For example, p(300) = 16.5 percent and q = 2.5 percent for $0^\circ \leq \theta \leq 10^\circ$. The standard error in Mev for this angular group is then $\Delta(E') = 10^{-2}\, E'\,(0.908\, E' + 6.3)^{1/2}$. If we take the neutron spectrum to be the unfolded spectrum of Fig. 11; then after following the procedure outlined in Appendix A 3 we find that 4.8 percent of the tracks in the interval $0^\circ \leq \theta \leq 10^\circ$ are expected to be missing as a result of the errors in measurement.

5. Loss of Neutrons through Lower Energy Boundary, Assuming Non-Gaussian Errors of Measurement

To estimate the number of neutrons above 200 Mev which are thrown into energies below 200 Mev from turbulence in the tracks we shall procede as follows. We have assumed previously, Appendix A 1, that the error in the measurement of the radius of curvature ρ_s of a track which is caused by turbulence is $\pm \rho_s/\rho_t$, where ρ_t is the radius of curvature arising from turbulence. We will proceed to show that this assumption is not valid unless $\rho_t \gg \rho_s$. Let us consider the cases

$$\frac{1}{\rho^+} = \frac{1}{\rho_s} + \frac{1}{\rho_t}$$

and

$$\frac{1}{\rho^-} = \frac{1}{\rho_s} - \frac{1}{\rho_t}$$

where ρ^+ and ρ^- are the radii of curvature measured. The fractional errors in the measurement of ρ_s are

$$\frac{\rho^+ - \rho_s}{\rho_s} = \frac{-\rho_s}{\rho_s + \rho_t} = -\left(\frac{\rho_s}{\rho_t}\right) - \left(\frac{\rho_s}{\rho_t}\right)^2 - \left(\frac{\rho_s}{\rho_t}\right)^3 - \cdots$$

$$\frac{\rho^- - \rho_s}{\rho_s} = \frac{-\rho_s}{\rho_s - \rho_t} = +\left(\frac{\rho_s}{\rho_t}\right) - \left(\frac{\rho_s}{\rho_t}\right)^2 + \left(\frac{\rho_s}{\rho_t}\right)^3 - \cdots$$

If $\rho_t \gg \rho_s$ the error is $\pm (\rho_s/\rho_t)$. However, if ρ_t is comparable to ρ_s this result is certainly not valid.

Let $C_t = 1/\rho_t$ be the curvature in a track which arises from turbulence. Also, let $P(C_t)dC_t$ represent the probability that a track will lie in an interval dC_t about C_t. The probability is normalized to unity by setting $\int_{-\infty}^{\infty} P(C_t)dC_t = 1$. The measured curvature C is related to the true curvature C' by $C = C' + C_t$. Suppose f(C') represents the distribution function for the curvatures of a group of tracks which

are to be measured. On account of the presence of turbulence f(C') will be measured as F(C) where

$$F(C) = \int_{C_1'}^{C_2'} P(C - C')f(C')\,dC'.$$

f(C') is assumed to be zero outside of the interval $C_1' \leqslant C' \leqslant C_2'$.

The number of neutrons with energies in the range $E_1' \leqslant E' \leqslant E_2'$ which are thrown into energies $E_1 \leqslant E \leqslant E_2$ by errors in curvature measurements corresponds to the number of tracks in the curvature spectrum of extent $C_1' \leqslant C' \leqslant C_2'$ which appear in the interval $C_1 \leqslant C \leqslant C_2$. The number is given by

$$N(C_1, C_2) = \int_{C_1}^{C_2} F(C)dC = \int_{C_1}^{C_2} \int_{C_1'}^{C_2'} P(C-C')f(C')dC'dC.$$

Now let us study two groups of tracks. The first group to be considered ($30^\circ \leqslant \theta \leqslant 40^\circ$, $45^\circ \leqslant \phi \leqslant 135^\circ$, $225^\circ \leqslant \phi \leqslant 315^\circ$) lie in squares (See Fig. 20.) which are symmetrically located about the excluded regions but removed one square from them. Let us define a representative track in this group by specifying its angles $\alpha = 35^\circ$ and $\beta = 0^\circ$. A second group to be considered ($40^\circ \leqslant \theta \leqslant 50^\circ$, $45^\circ \leqslant \phi \leqslant 135^\circ$, $225^\circ \leqslant \phi \leqslant 315^\circ$) lie in squares adjacent to the excluded regions. Let us define a representative track in this group by stating its angles $\alpha = 45^\circ$ and $\beta = 0^\circ$. The slant radius of curvature ρ_s for any track is given by the expression

$$\rho_s = \frac{\rho \cos \beta}{1 + \frac{T_n}{1876} \sin^2 \theta} \tag{7}$$

where

$$\rho = \frac{10^4}{3B} \left[T_n (T_n + 1876) \right]^{1/2} \tag{8}$$

It can be shown by calculations that the two representative tracks have nearly the same slant radii of curvature for the same neutron energy

$E' = T_n$. From the point of view of making error calculations on these tracks, even a different choice of β other than the one we have employed (as long as β is not too large) will not appreciably affect the results. If we assume that $B = 21,700$ gauss we can calculate $C' = 1/\rho_s$ for, say, $\alpha = 45^o$ and $\beta = 0^o$. The curvature spectrum $f(C')$, Fig. 19, is constructed from the unfolded energy spectrum $f(E')$, Fig. 11. The values of C_1' and C_2' that correspond to the values $E_1' = 200$ Mev and $E_2' = 340$ Mev are $C_1' = 0.01064$ cm.$^{-1}$ and $C_2' = 0.00818$ cm.$^{-1}$. The number of missing tracks for either group of tracks mentioned is then

$$\int_{0.01064}^{\infty} dC \int_{0.00818}^{0.01064} f(C')P(C-C')dC'$$

Fig. 19 shows the form assumed for $P(C_t)$. Since $\int_{-\infty}^{\infty} P(C_t)dC_t = 1$ we have $AB = 1$.

Consider the first group of tracks mentioned above. No tracks in this group were ever observed to curve the wrong way in the magnetic field so we assume that $\rho_t \geqslant 120$ cm. However, measurements (Lucite-template method on tracks in no-field pictures) on the turbulence for this group of tracks disclose values of ρ_t up to 120 cm., although some of these tracks appear perfectly straight. We assume $B = 1/120$ cm.$^{-1}$ for this group.

Consider the second group of tracks mentioned above. No tracks in this group possessed a turbulence curvature $\rho_t \leqslant 400$ cm. so we assume $B = 1/400$ cm.$^{-1}$ for this group.

The results of the calculations show that 10 percent of the tracks in the first group are lost through errors in measurement of the neutron energy while the corresponding figure for the second group is 36 percent.

APPENDIX B

1. Derivation of Equations (2), (5) and (6) which Appear in the Text

Equations

$$\cos \theta = \cos \alpha \cos \beta \tag{2}$$

and

$$\tan \phi \sin \beta = \tan \alpha \tag{5}$$

may be derived from a consideration of Fig. 23. The line OP represents the tangent to a track which starts at the origin 0. The line OQ represents the direction of the neutron beam.

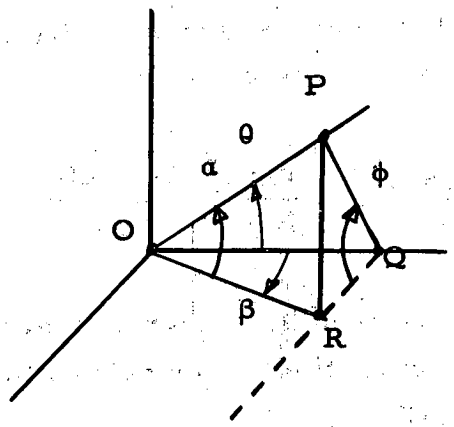

Fig. 23

$$\cos \theta = \frac{OQ}{OP} = \frac{OR}{OP} \cdot \frac{OQ}{OR} = \cos \alpha \cos \beta$$

$$\tan \alpha = \frac{RP}{OR} = \frac{RP}{QR} \cdot \frac{QR}{OR} = \tan \phi \sin \beta$$

Now we will derive the equation for the weighting factor

$$f(\theta, \alpha_o) = \frac{\pi/2}{\sin^{-1} (\sin \alpha_o / \sin \theta)} \tag{6}$$

First we must derive the equation

$$\sin \alpha = \sin \theta \sin \phi$$

by considering Fig. 23 once more:

$$\sin \alpha = \frac{PR}{OP} = \frac{PR}{QP} \cdot \frac{QP}{OP} = \sin \phi \sin \theta$$

A plot of the equation $\sin \alpha = \sin \theta \sin \phi$ is given for the case $\alpha = 40^{o}$ in Fig. 24. If only tracks for which $\alpha \leqslant \alpha_o = 40^{o}$ are measured, then the remaining tracks lie in the excluded region bounded by the curve. Now consider any limiting dip angle α_o. Let $N_M(\theta)$ be the number of tracks measured outside the excluded region for a small band of θ. Assume azimuthal symmetry. The total number of tracks $N_T(\theta)$ (including those in the excluded region) is given by $f(\theta, \alpha_o)N_M$ where $f(\theta, \alpha_o)$ is a weighting factor to be determined. By considering Fig. 24 once more we can easily show

$$f(\theta, \alpha_o) = \frac{N_T}{N_M} = \frac{4A + 4B}{4A} = \frac{A + B}{A} = \frac{\pi/2}{\sin^{-1} (\sin \alpha_o / \sin \theta)}$$

It is also evident from the diagram that $f(\theta \leqslant \alpha_o, \alpha_o) = 1$. The maximum value for the correction factor occurs for $\theta = 90^{o}$ and has the value $f(90^{o}, \alpha_o) = \pi/(2\, \alpha_o)$.

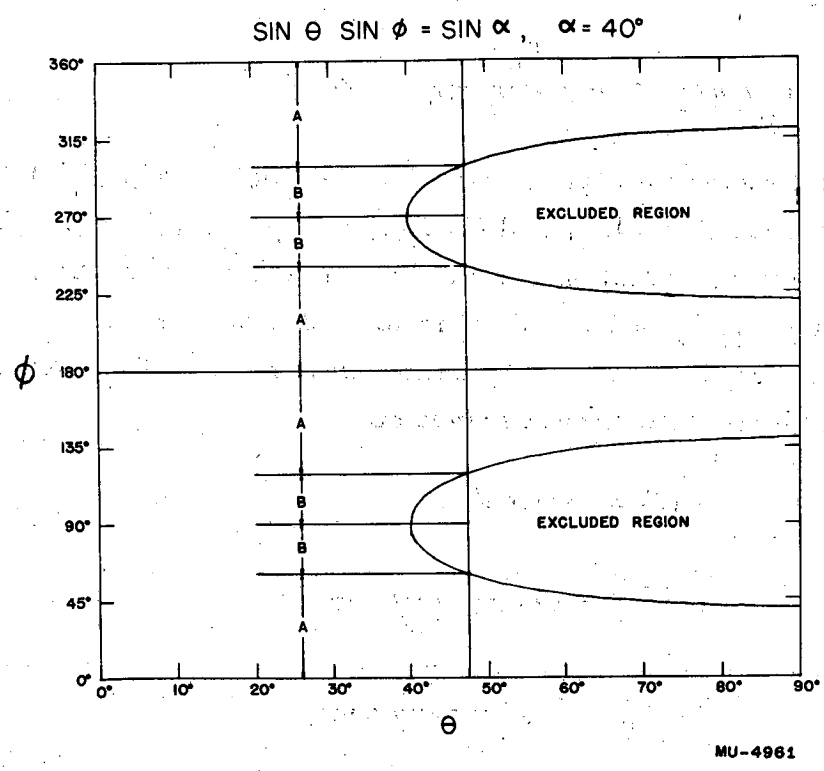

Fig. 24 A plot of the equation sin θ sinφ = sin 40° is given. The curve encloses the excluded region and contains those tracks whose dip angles are greater than 40°. The diagram is employed in the derivation of equation (6) which is given in the text.

APPENDIX C

Nomographs

1. Nomograph for Calculation of the Neutron Energy

Fig. 25 shows two sets of nomographs for the formula (3) which may be put in the form

$$\frac{T_p}{1 + T_p/1876} = \frac{T_n}{1 + T_n/1876} \cos^2 \theta$$

Consider the following two type forms[16] of nomographs (1) $f_1(u) + f_2(v) = f_3(w)$ (three parallel scales) and (2) $f_1(u) = f_2(v)f_3(w)$ (two parallel scales and a slanting scale) where the scales are to be labeled in terms of u, v and w and f_1, f_2 and f_3 are functions of these variables. The discussion now will be presented in outline form only and the equations[16] employed will be listed without derivation.

Type 1 Let $f_1(\theta) = \log \cos^2 \theta$

$$f_2(T_n) = \log \frac{T_n}{1 + T_n/1876}$$

$$f_3(T_p) = \log \frac{T_p}{1 + T_p/1876}$$

where $u = \theta$, $v = T_n$, $w = T_p$

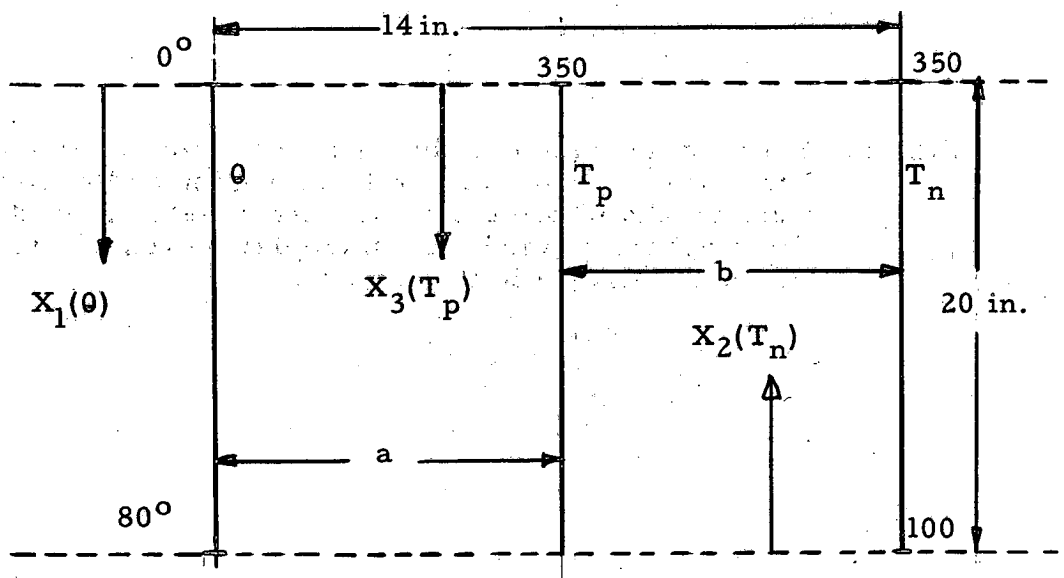

Fig. 26

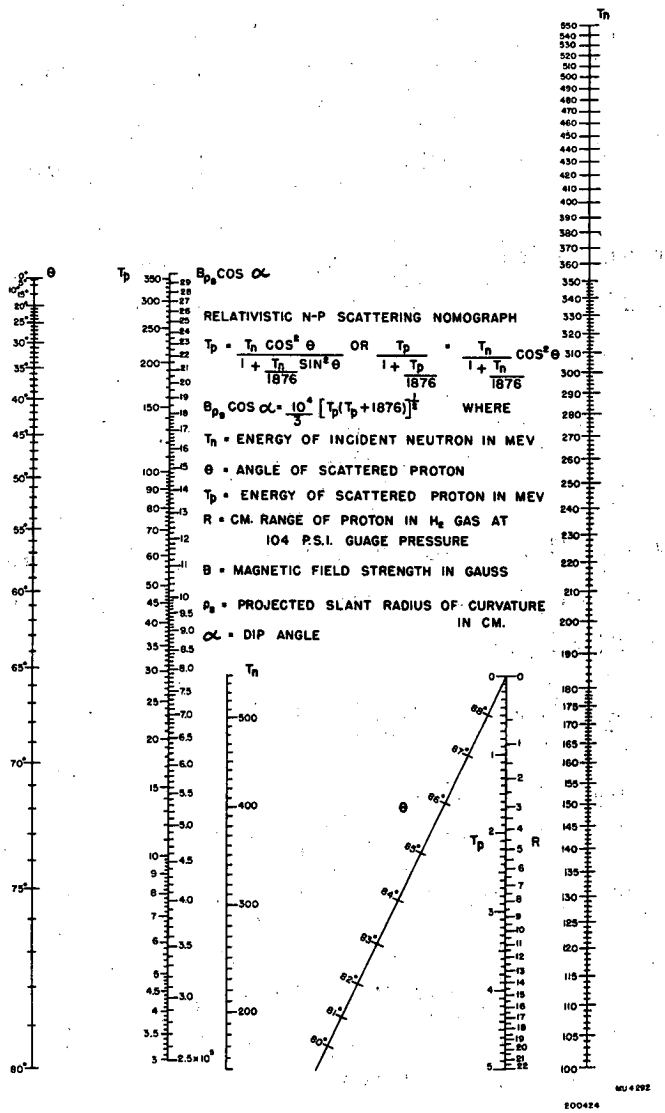

Fig. 25 Nomograph for calculation of the neutron energy.

The scale equations (See Fig. 26 for definitions.) are

$$X_1(\theta) = m_1 \left[f_1(0^\circ) - f_1(\theta) \right]$$

$$X_2(T_n) = m_2 \left[f_2(T_n) - f_2(100) \right]$$

$$X_3(T_p) = m_3 \left[f_3(T_p) - f_3(100) \right]$$

and the two scale factors m_1 and m_2 are determined by setting $X_1(80^\circ) = X_2(350) = 20$ in., while the remaining scale factor m_3 is calculated from the equation

$$m_3 = \frac{m_1 m_2}{m_1 + m_2}$$

Let the width of the nomograph be $a + b = 14$ in., then the scale spacings a and b are calculated according to the formula $a/b = m_1/m_2$. The results of the calculations are

$m_1 = 13.152$, $m_2 = 40.621$, $m_3 = 9.935$, $a = 3.424$ in.

and $b = 10.576$ in.

Type 2 Let

$$f_1(T_n) = \frac{T_n}{1 + T_n/1876}$$

$$f_2(T_p) = \frac{T_p}{1 + T_p/1876}$$

$$f_3(\theta) = \cos^2 \theta$$

where $u = T_n$, $v = T_p$, $w = \theta$

The scale equations (See Fig. 27 for definitions.) for T_n and T_p are

$$X_1(T_n) = m_1 \left[f_1(T_n) - f_1(150) \right]$$

$$X_2(T_p) = m_2 \left[f_2(T_p) - f_2(0) \right]$$

The location of the slanting scale for θ is determined by specifying the distance b (See Fig. 27) where b is calculated from the equation

$$b = \frac{c\, m_1\, f_1\,(150)}{a + m_1 f_1\,(150)}$$

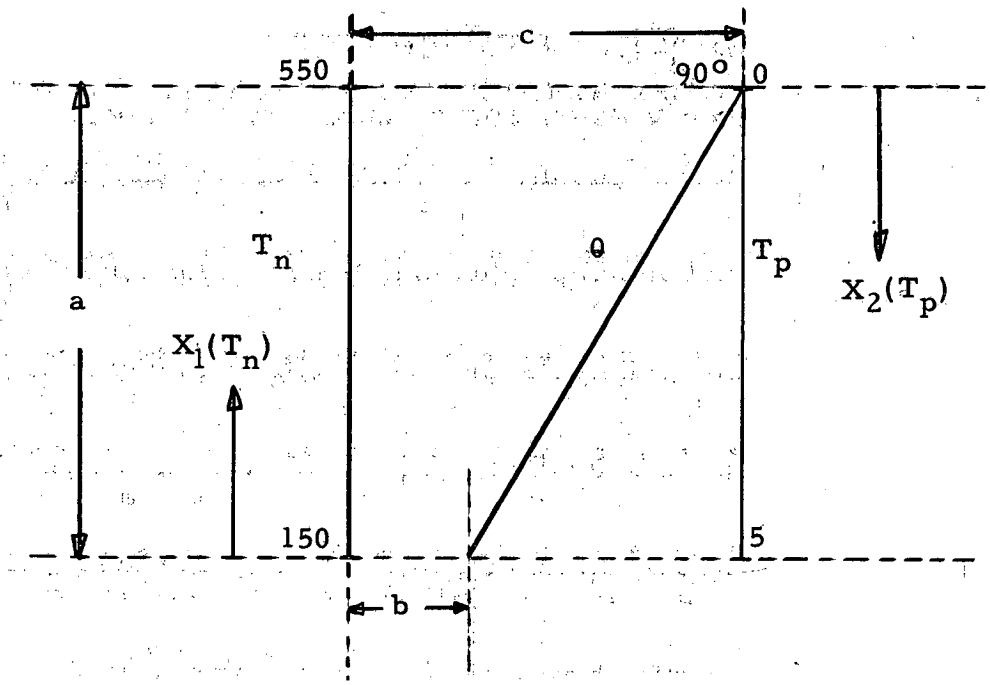

Fig. 27

By taking $a = X_1(550) = X_2(5) = 10$ in. and letting $c = 7$ in. the scale factors m_1 and m_2 and the spacing b are calculated to be $m_1 = 0.03391$, $m_2 = 2.002$ and $b = 2.241$ in. The scale for θ is labeled in one degree steps by calculating values of T_n and T_p and then drawing straight lines across the nomograph through these values to intersect the θ scale.

In each nomograph the scales for T_p are also labeled with values of $B\rho_s \cos\alpha$ or range R so that T_p need not be calculated in applying the nomographs to the experimental data obtained for this paper.

Figure 28 shows two superimposed scales from which one may evaluate the kinetic energy T for a proton, providing its magnetic rigidity is known.

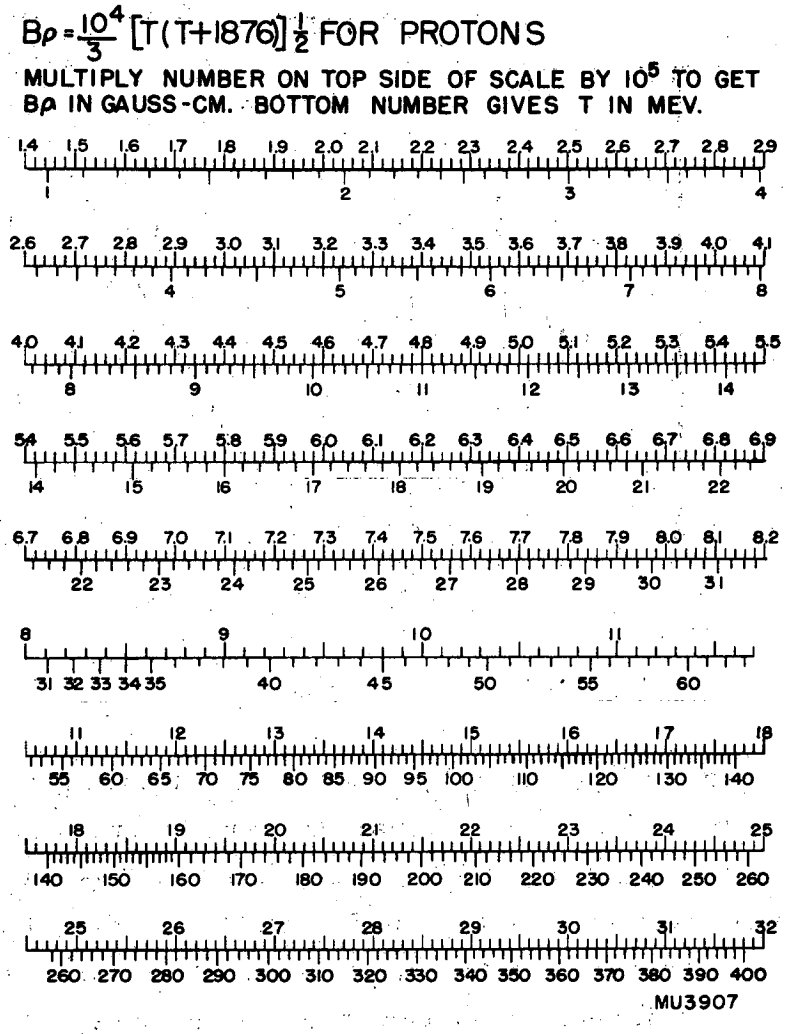

Fig. 28 Chart giving Bρ vs. kinetic energy for protons.

Circular Nomographs

Figure 29 shows a sketch of a circular[17] nomograph which will be used presently to represent an equation of the form W = UV.

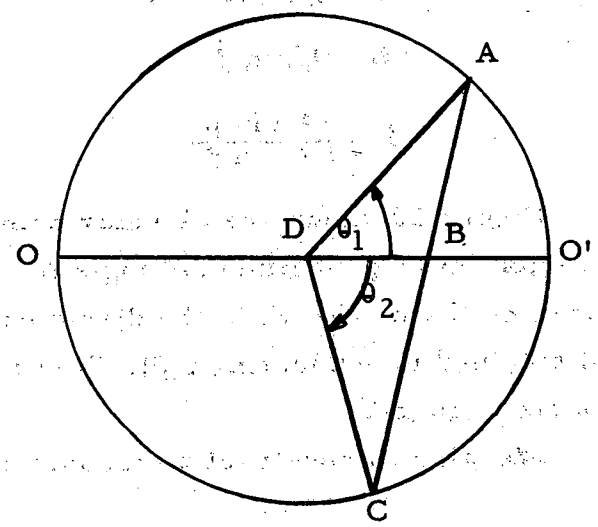

Fig. 29

A circle of radius A = OD = DO' has been described about the point D. The line AC intersects the diameter OO' at the point B. One can derive an expression for S = OB in terms of the radius A and the central angles θ_1 and θ_2. The result is

$$S = \frac{2A}{1 + \tan\frac{\theta_1}{2}\tan\frac{\theta_2}{2}}$$

Let $U = \tan \theta_1/2$, $V = \tan \theta_2/2$, and $W = UV$, then

$$S = \frac{2A}{1 + W}$$

We wish to construct a circular nomograph for the equation

$$\tan \phi \sin \beta = \tan \alpha \qquad (5)$$

which appears in the text. Let $\theta_1 = 2\phi$ and $\theta_2 = 180 - 2\alpha$, then the

following equations

$$U = \tan \phi$$

$$V = \tan (90 - \alpha)$$

$$W = 1/\sin \beta$$

$$S = \frac{2A \sin \beta}{1 + \sin \beta}$$

hold true. Figure 30 shows the circular nomograph which was employed for the calculation of the azimuthal angle ϕ. The uniform scales for α and ϕ appear on the circle while the diameter contains the non-uniform scale in β obtained by evaluating $S(\beta)$. The radius of the life-size nomograph was seven inches.

We wish to construct a circular nomograph for the equation

$$\tan \theta = \frac{\cot \theta'/2}{\left(1 + \frac{T_n}{1876}\right)^{1/2}} \qquad (4)$$

which appears in the text. Let $\theta_1 = 2\theta$ and $\theta_2 = \theta'$, then the following equations hold true:

$$U = \tan \theta$$

$$V = \tan \theta'/2$$

$$W = \left(1 + \frac{T_n}{1876}\right)^{1/2}$$

$$S = \frac{2A}{1 + \left(1 + \frac{T_n}{1876}\right)^{-1/2}}$$

Figure 31 shows the circular nomograph which was employed for the calculation of the neutron angle in the center of mass system. The uniform scales for θ and θ' appear on the circle while the diameter contains the non-uniform scale in T_n obtained by calculating $S(T_n)$. The radius of the life-size nomograph was seven inches.

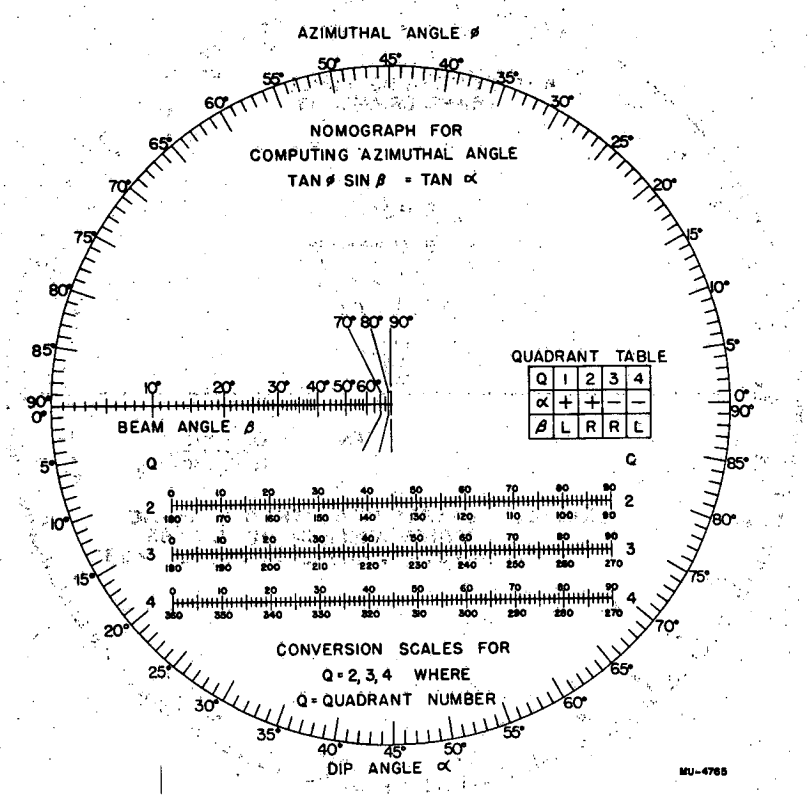

Fig. 30 This nomograph may be employed to determine the azimuthal ϕ angle from the dip angle α and the beam angle β.

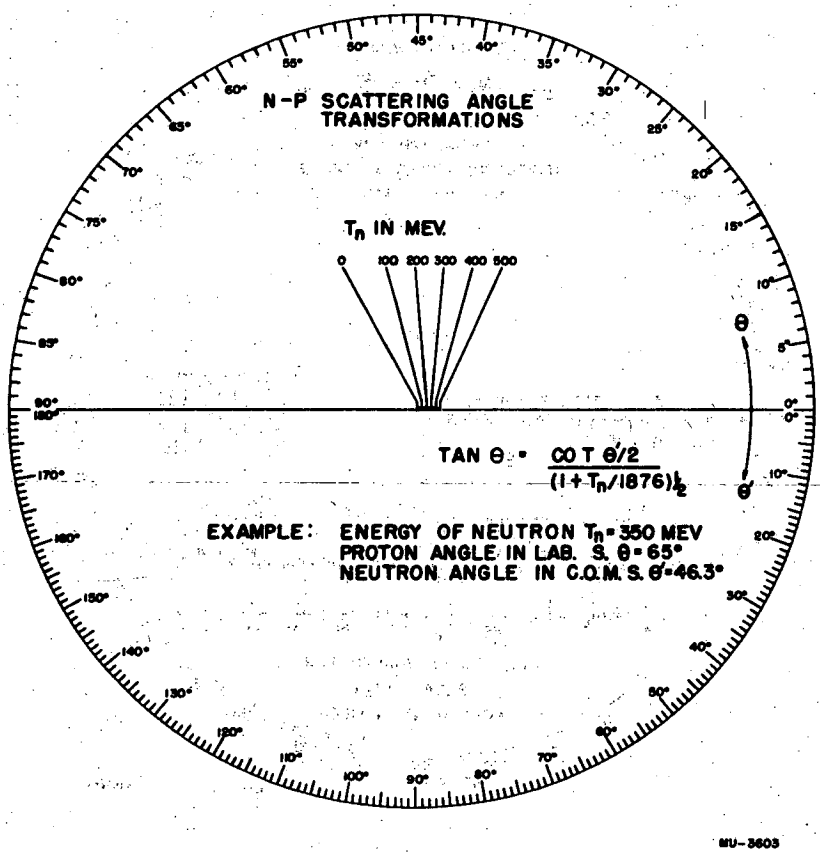

Fig. 31 This nomograph may be used to determine the neutron angle in the center of mass system from the proton angle in the laboratory system as a function of the energy of the incident neutron.